Karlsruher Institut für Technologie

ETP-KA/2021-12

Laboratory and Integration Tests with 2S Module Prototypes for the Phase-2 Upgrade of the CMS Outer Tracker

Labor- und Integrationstests mit 2S Prototypmodulen für das Ausbauprogramm des CMS-Spurdetektors

Master Thesis
by

Lea Stockmeier

at the Institute of Experimental Particle Physics

Reviewer:	Prof. Dr. Ulrich Husemann
Second Reviewer:	Prof. Dr. Thomas Müller
Advisor:	Dr. Alexander Dierlamm
Second Advisor:	Roland Koppenhöfer

Karlsruhe, 30.09.2021

Lea Stockmeier:
Laboratory and Integration Tests
with 2S Module Prototypes
for the Phase-2 Upgrade
of the CMS Outer Tracker
September 2021

This thesis has been accepted by the first reviewer of the master thesis.
Karlsruhe, 30 September 2021

. . . . . .
(**Prof. Dr. Ulrich Husemann**)

I hereby certify that the enclosed thesis is my own work, that I have not sought or used inadmissible help of third parties to produce this work and that I have clearly referenced all sources used in the text.

Karlsruhe, 30 September 2021

. . . . . .
(**Lea Stockmeier**)

Contents

Part I.

Introduction and Basics

1 Introduction

With the discovery of the Higgs boson in 2012, the last particle of the Standard Model of Particle Physics was discovered by the ATLAS[1] and CMS[2] experiments at the CERN[3] *Large Hadron Collider* (LHC). Physicists and engineers from all over the world worked together to reach this milestone in modern particle physics. The goal of research at the LHC is to discover new physics. For that purpose, it will be upgraded to the *High-Luminosity LHC* (HL-LHC) until 2027. As indicated by the name, the luminosity will be increased after the upgrade, meaning an increase in the number of expected collisions. Thus, the discovery potential for physics with very small event rates will be increased compared to the current LHC.

With increased luminosity, the particle density and radiation exposure of the detectors mounted around the four interaction points will be enlarged. Thus, the experiments at the LHC will be upgraded as well. For the CMS experiment this is called the *CMS Phase-2 Upgrade*. Within this upgrade, the tracker of the CMS experiment will be fully replaced. The new tracker will be divided into two parts, the Inner Tracker and the Outer Tracker. The outermost part of the Outer Tracker will be equipped with silicon detector modules with two silicon strip sensors each aligned in parallel. These modules are called 2S modules. With this module geometry, it is possible to filter events with high transverse momentum particles already on module level. This information is used as input for the *Level-1* trigger system of the CMS experiment while the full data is stored for the final trigger decision.

The 2S modules for the *CMS Phase-2 Outer Tracker Upgrade* will be built at eight assembly centers. One of these assembly centers is the *Institute of Experimental Particle Physics* (ETP) at the *Karlsruhe Institute of Technology* (KIT), which will assemble 1500 to 2000 2S modules. Currently, prototype modules are built. With these modules, the assembly procedure is validated and exercised and functional tests are performed.

Within this thesis, two setups for laboratory and integration tests are designed and the results of the first measurements are presented. In the 2S muon hodoscope described in Chapter 4, up to three modules can be stacked. With this geometry, it is possible to track cosmic muons and to reconstruct the muon signal charge. The synchrony and long term stability of the module readout can be checked as well.

The second setup presented in this thesis is called the *KArlsruhe LAdder MOckup* (KALAMO). It is explained in detail in Chapter 5. The idea of this setup is to mount the modules in the same arrangement as in the later CMS Phase-2 Outer Tracker. It can be tested if one module picks up disturbances by the other two modules. The setup is designed in such a way that all currently investigated prototype modules can be mounted.

Chapter 2 introduces the LHC and its upgrade to the HL-LHC as well as the CMS experiment and the CMS Phase-2 Outer Tracker Upgrade. The working principle of semiconductor particle detectors and the interaction of particles with matter is introduced briefly in Chapter 3 while Section 3.3 describes the 2S modules for the CMS Phase-2 Outer Tracker Upgrade in more

[1] A Toroidal LHC Apparatus
[2] Compact Muon Solenoid
[3] European Organization for Nuclear Research (french: Conseil Européen pour la Recherche Nucléaire)

detail. A description of the experimental setups and results of measurements with the 2S muon hodoscope and KALAMO are presented in the main part in Chapters 4 and 5.

2

The Large Hadron Collider and the Compact Muon Solenoid Experiment

This chapter briefly introduces the experimental background of this thesis. Section 2.1 provides information about the Large Hadron Collider (LHC) while Section 2.2 describes the Compact Muon Solenoid (CMS) Experiment which is located at the LHC. Both the LHC and the CMS experiment will be upgraded starting in 2025. The upgrade plans are presented in Section 2.3.

2.1. The Large Hadron Collider

The *Large Hadron Collider* (LHC) is a proton and heavy ion accelerator located at the *European Organization for Nuclear Research* (CERN, french: *Conseil Européen pour la Recherche Nucléaire*) in Switzerland. Its storage ring is 100 m under ground and has a circumference of almost 27 km. There are two beampipes with counter-rotating proton beams. Both beams can reach an energy of 7 TeV which leads to a possible collision center-of-mass-energy of $\sqrt{s} = 14\,\text{TeV}$.

The proton acceleration to 7 TeV is reached by a chain of different accelerators which are part of the CERN accelerator complex (see Figure 2.1). The protons, which are extracted from hydrogen atoms via an electric field, are accelerated by the *Linear Accelerator 2* (Linac2) to an energy of 50 MeV. The *Proton Synchrotron Booster* (PSB) accelerates the protons to an energy of 1.4 GeV while the next part of the chain, the *Proton Synchrotron* (PS), reaches proton energies of 25 GeV. The last step before injecting the particles into the LHC is the *Super Proton Synchrotron* (SPS), where the protons are accelerated to an energy of 450 GeV. [Ben+04]

At the LHC a bunched particle beam is accelerated by radiofrequency cavities via an oscillating electromagnetic field at 400 MHz. This results in bunches of particles with equal energy. The nearly circular trajectory is achieved by 1232 superconducting dipole magnets, having magnetic fields up to 8.33 T. The beam focussing is provided by additional multipole magnets of higher orders. The superconducting state is kept by cooling the radiofrequency cavities and dipole magnets down to 1.8 K with liquid helium. [Brü+04]

There are four interaction points where the two beams can be brought to collision. At each of these points, a physics experiment is placed around the beam pipe to detect the resulting particles of the collision. *A Large Ion Collider Experiment* (ALICE) investigates the properties of quark-gluon plasma in heavy ion collisions. *A Toroidal LHC Apparatus* (ATLAS) and the *Compact Muon Solenoid* (CMS) Experiment are the two general-purpose detectors at the LHC. Testing QCD, electroweak interactions and flavour physics are goals of both experiments. The different technical solutions, which are incorporated in these two experiments, allow a cross-check of the results. With the discovery of the Higgs boson in 2012, one of their scientific goals is achieved. The fourth experiment, *Large Hadron Collider beauty* (LHCb), gets a deeper look into B-physics and can thus get information about the matter-antimatter asymmetry.

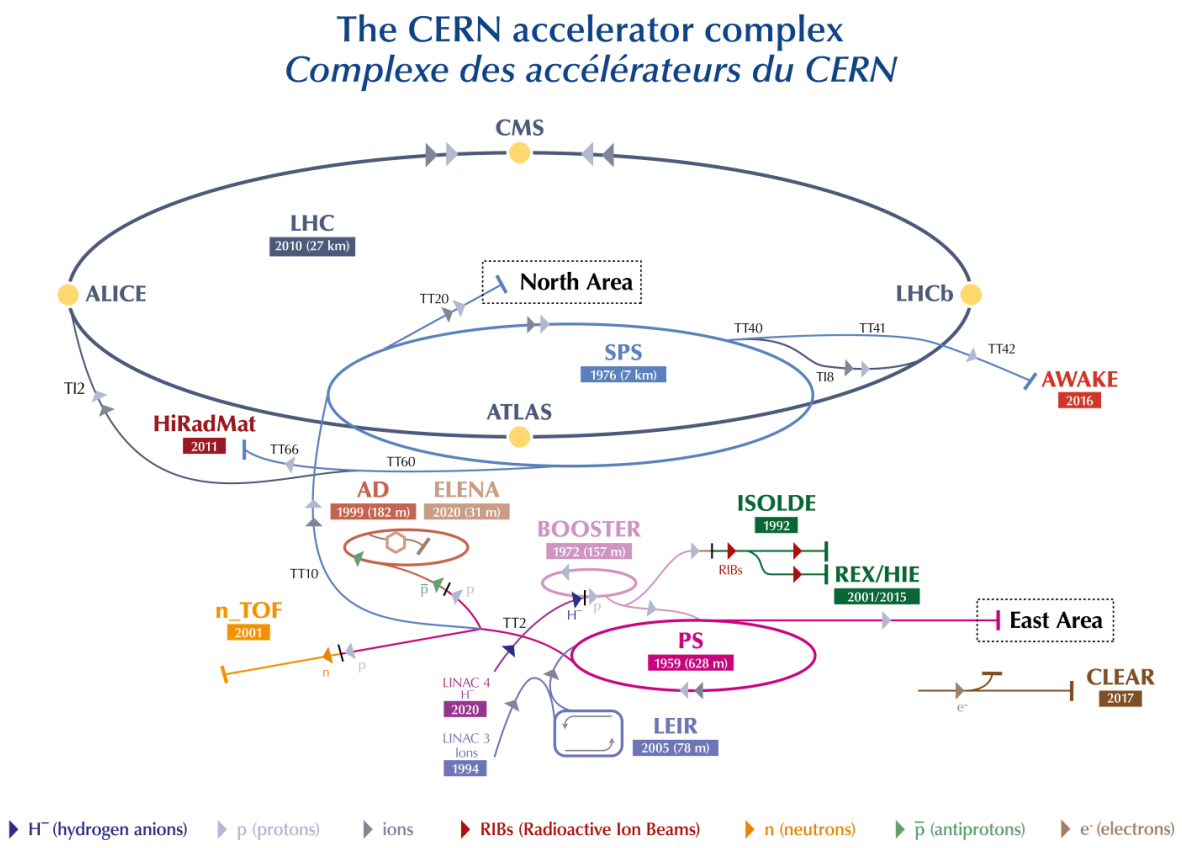

Figure 2.1.: The CERN accelerator complex. The Linear Accelerator 2 (Linac2), Proton Synchrotron Booster (PSB), Proton Synchrotron (PS) and Super Proton Synchrotron (SPS) are the four pre-accelerators of the LHC. [Mob19]

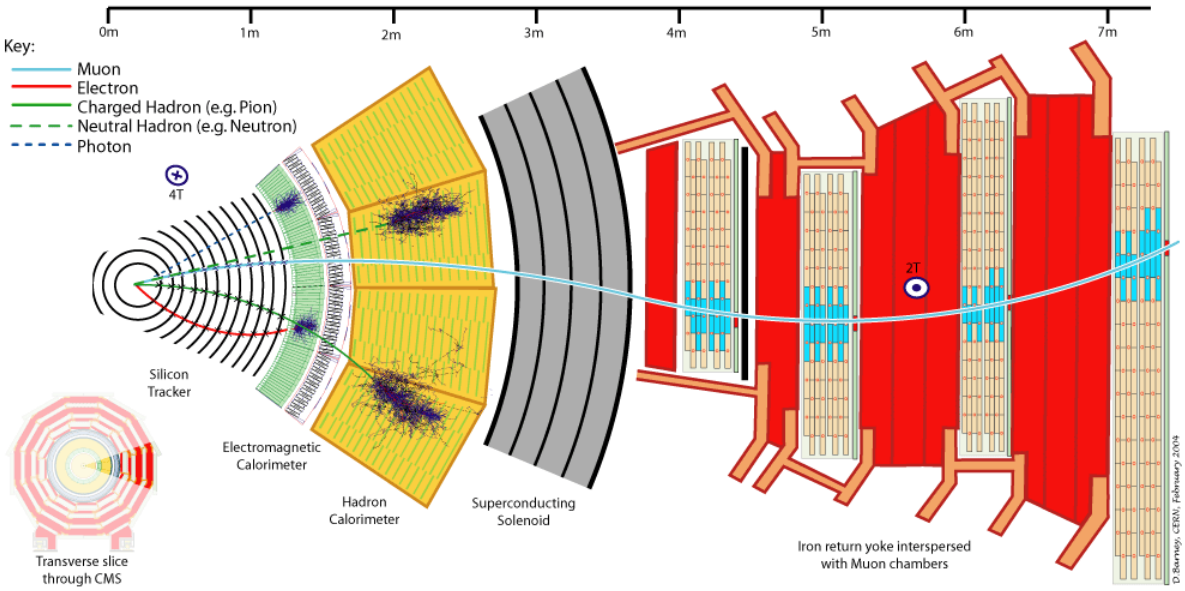

Figure 2.2.: Illustration of the CMS experiment. The small picture on the lower left depicts a transverse slice through the CMS experiment. The largely shown sector is indicated. The different sub-detectors from inner to outer part are the silicon tracker, the electromagnetic calorimeter, the hadron calorimeter, the superconducting solenoid and the muon system with steel return yokes. Tracks of different particles and their interaction with the sub-detectors are depicted as well. [Dav16]

2.2. The Compact Muon Solenoid Experiment

With a mass of 14,000 t, a diameter of 15 m and a length of 29 m, the *Compact Muon Solenoid* (CMS) experiment is the heaviest and second largest experiment at the Large Hadron Collider. [CMS08]

For the purpose of particle identification, the CMS experiment is constructed with different sub-detector systems arranged in cylindrical layers around the beam-pipe. The interaction point is in the center of this cylindrical detector. A schematic view of a sector of the CMS experiment can be seen in Figure 2.2. Each layer has a different task in the identification of the particles resulting from the proton-proton or ion-ion collisions. The silicon tracker consists of two parts, one made of pixel modules and the other made of strip modules. Together, they determine the trajectory of charged particles. The electromagnetic calorimeter (ECAL) measures the energy of electromagnetically interacting particles, while the hadron calorimeter (HCAL) is responsible for the energy measurement of strongly interacting particles. All these detector parts are situated within a superconducting solenoid with a magnetic field of 3.8 T to bend the trajectories of charged particles. The outermost part of the CMS experiment is the muon system for detecting muons and determine their trajectories. In between the muon chambers lies a steel return yoke to guide the outer magnetic field lines. [CMS08]

Figure 2.3.: Timetable of the LHC and HL-LHC project from 2011 to 2040. During the *Run* phases data are taken while the *Long Shutdowns* (LS) allow the installation of new detector systems in the experiments. [CER21]

2.3. The High-Luminosity LHC Upgrade and the CMS Phase-2 Outer Tracker Upgrade

To investigate e.g. physics beyond the standard model with very small event rates, the luminosity of the LHC will be increased. For that purpose, the LHC is upgraded to the *High-Luminosity LHC* (HL-LHC). This upgrade is planned to be installed until 2027. With the increased luminosity, also the experiments at the LHC have to be upgraded to withstand the radiation exposure during the lifetime of the HL-LHC. Section 2.3.1 describes upgrade plans of the LHC while Section 2.3.2 introduces the CMS Phase-2 Outer Tracker upgrade.

2.3.1. The High-Luminosity LHC Upgrade

The central aim of the HL-LHC upgrade is the increase of the collision rate. This will be achieved by increasing the instantaneous collision rate by a factor of five compared with the LHC nominal design values. It is aimed to reach instantaneous peak luminosities up to $7.5 \times 10^{34}\,\mathrm{cm^{-1}s^{-1}}$ in the ultimate performance scenario. This increases the delivered integrated luminosity as well. Thus, the integrated luminosity will reach $3000\,\mathrm{fb}^{-1}$ to $4000\,\mathrm{fb}^{-1}$ by the end of Run 3. The bunch spacing will remain 25 ns at a center-of-mass-energy of 14 TeV. [Béj+20]

The schedule of the upgrade plans and measuring periods of the LHC and HL-LHC can be seen in Figure 2.3. The main parts of the HL-LHC upgrade are planned to be installed during *Long Shutdown 3* (LS3), which will take place from 2025 to mid of 2027. Some other parts are installed during *Long Shutdown 2* (LS2) which started in 2019 and will take until the first quarter of 2022. [Béj+20]

The triplet quadrupole magnets need to be replaced. The radiation hardness of the updated version is increased due to the new superconducting intermetallic compound of niobium and tin (Nb_3Sn). The critical current is higher in Nb_3Sn compared to that of niobium-

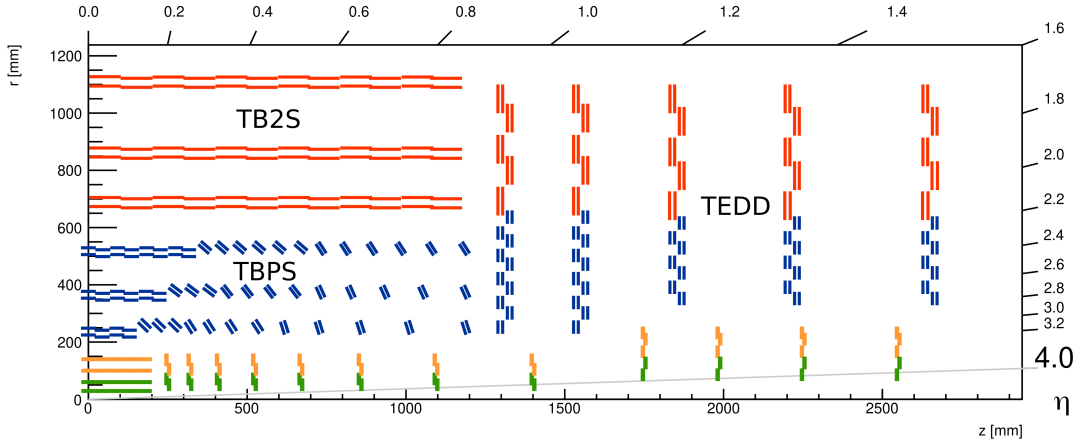

Figure 2.4.: Illustration of one quarter of the CMS tracker after the Phase-2 Upgrade. The interaction point is located at the origin of coordinates. The silicon pixel modules of the CMS Inner Tracker are depicted in yellow and green while the modules of the CMS Outer Tracker are shown in blue (PS modules) and red (2S modules). The Outer Tracker is subdivided into the Tracker Barrels (TB) and the Tracker Endcap Double-Discs (TEDD). The inner Tracker Barrels consist of PS modules (TBPS) and the outer of 2S modules (TB2S). The TEDDs are equipped with 2S and PS modules. Adapted from [CMS17].

titanium (NbTi) which is used for the current triplet quadrupole magnets. Crab cavities are inserted to increase the beam profile overlap area which increases the probability of collisions and, thus, the luminosity. Additional collimators are needed to protect the machine by absorbing particles that stray from the beam. To get place in the LHC ring for the insertion of the collimators, two dipole magnets for bending the trajectory of accelerated particles are replaced by two pairs of shorter magnets. [CERb] Upgrades in the injector chain are also needed. For example, Linac2 was replaced by the *Linear accelerator 4* (Linac4) in 2020. It accelerates negative hydrogen ions (H^-) to 160 MeV. [CERa]

2.3.2. The CMS Phase-2 Outer Tracker Upgrade

Due to the higher luminosity expected of the HL-LHC, the radiation exposure of the detector parts as well as the number simultaneous interactions per bunch crossing, called pileup, will also increase. There are 140 to 200 pileup events expected for the HL-LHC [Sch16]. Most of the currently mounted detector parts of the CMS experiment have to be upgraded to comply with the new requirements of the detector. One of these parts is the CMS tracker, which will be fully replaced during the *Long Shutdown 3*. The Inner Tracker will consist of silicon pixel modules and the Outer Tracker will be made of silicon strip and macro-pixel modules. Figure 2.4 shows an illustration of one quarter of the CMS tracker after the Phase-2 Upgrade. The Outer Tracker consists of PS (pixel-strip) and 2S (strip-strip) modules. In the *Tracker Barrel* (TB) most of the modules are arranged in cylindrical layers. The outer TB is equipped with 2S modules (TB2S) and the inner with PS modules (TBPS). The endcap is made of discs, called *Tracker Endcap Double-Discs* (TEDD). The arrangement of the 2S modules in the Outer Tracker is described more detailed in Section 3.3.4. [CMS17]

The most important innovation of the Phase-2 Outer Tracker is to provide input for the *Level-1* (L1) trigger. The aim of the L1 trigger is to select physically interesting events. One criterion is to select events including particles with transverse momenta p_T higher than 2 GeV/c.

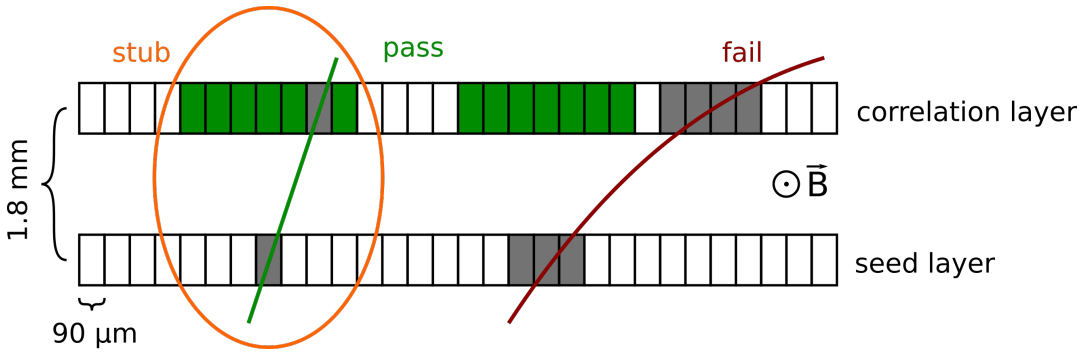

Figure 2.5.: Illustration of stub finding logic. The combination of two clusters is called a *stub* if their spatial displacement lies within a predefined stub window. The channels comprising the stub window are depicted in green. Particles with high transverse momentum (little bent trajectories in magnetic field) produce stubs (on the left) while particles with low transverse momentum do not lead to stubs (on the right).

This cut is provided by the Outer Tracker. Due to the magnetic field of 3.8 T, trajectories of particles with high transverse momentum are bent less than particle trajectories with lower transverse momentum. To get information about the bend and thus the transverse momentum during the time between two bunch crossings, a module geometry with two parallel stacked silicon sensors is developed. These modules are described in detail in Section 3.3. Both sensors are read out with the same set of chips. Thus, the chips can combine the hit information of both sensors to *stubs*, which is illustrated in Figure 2.5. A stub is a combination of two clusters, one belonging to each sensor. If the spatial displacement of the clusters belonging to a stub is lower than the user-defined stub window, the stub is valid and read out. The information about the presence of a stub with small enough displacement is used as input for the L1 trigger. By adjusting the stub window, different minimum transverse momentum criteria can be selected for the trigger. [CMS17]

3
2S Modules for the CMS Phase-2 Outer Tracker

The CMS Phase-2 Outer Tracker is made of silicon strip and pixel modules. By the interaction of particles with the semiconductor material of the modules, they are able to detect the trajectories of charged particles. This chapter explains briefly the theory of semiconductor particle detectors in Section 3.1 while it describes the interaction of particles with matter in Section 3.2. Section 3.3 describes the 2S modules for the CMS Phase-2 Outer Tracker.

3.1. Basics of Semiconductor Particle Detectors

Since silicon detector modules are used in the tracker of the CMS experiment, the basics of semiconductor particle detectors are essential for this thesis. The energy band model, the principle of doping semiconductors and the pn-junction are explained as well as the basics of silicon strip detectors. The section is based on [Dem16].

3.1.1. The Energy Band Model

The energy levels of electrons in a single atom can be described as atomic orbitals. Each atomic orbital is characterized by a discrete energy level. When two atoms form a molecule, their atomic orbitals overlap, which leads to new energy states that allow the electrons to occupy additional energy states. The presence of more than one electron in the same energy level is forbidden due to the Pauli principle for fermions. A solid is formed by many atoms of the same type arranged in a crystalline lattice. The principle of overlapping energy levels leads to quasi-continuous electron energy levels. The allowed states (bands) are separated by so-called band gaps.

The temperature-dependent Fermi-Dirac distribution is the filling scheme for the energy bands. At $T = 0\,\mathrm{K}$ all energy levels up to the Fermi energy are occupied. The highest fully occupied energy band is called the *valence band*, while the next higher band is called the *conduction band*. The energy band gap for three types of solid material is depicted in Figure 3.1. For *semiconductors* and *insulators*, the Fermi energy lies within a band gap. Depending on the width of the energy gap, materials can be classified as insulators with a gap larger than $4\,\mathrm{eV}$, while the energy gap of semiconductors can vary from $1\,\mathrm{eV}$ to $4\,\mathrm{eV}$. This small band gap allows electrons to jump to the conduction band through thermal excitation at room temperature. The Fermi energy of *conductors* lies within the conduction band.

3.1.2. Doping of Semiconductors and pn-Junction

The principle of *doping* is to introduce atoms of other materials into the semiconductor's lattice. There are two types of doping: n- and p-doping. For silicon, the n- and p-doping is illustrated in Figure 3.2. If the number of valence electrons of the introduced atoms is larger than the one of the semiconductor atoms, it is called n-doping. In case of n-doping, the atoms of the

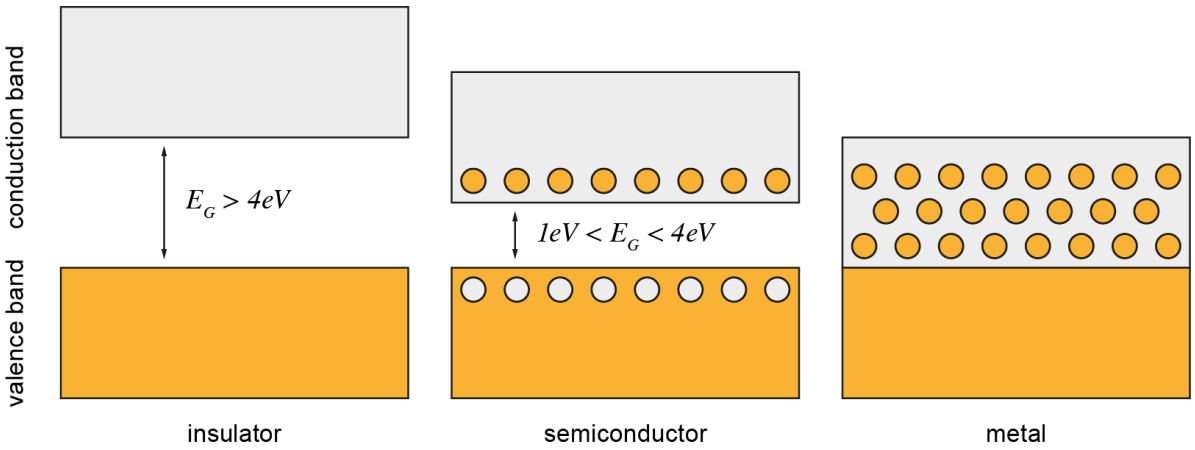

Figure 3.1.: Illustration of the energy band gap. The picture illustrates the energy band gap of insulators, semiconductors and metals. The valence band is depicted in orange while the conduction band is represented in light gray. Electrons belonging to the conduction band are illustrated as orange dots while holes in the valence band are indicated as white dots. [Bra20]

injected material are called *donors* because they add more valence electrons to the crystal than are needed for the covalent bonds of the lattice. Thus, the binding energy of the excess electron is relatively small, resulting in a new energy level in the band gap near to the conduction band minimum. It is filled with the excess electrons belonging to the doping material. The energy needed for the excitation to the conduction band of the electrons belonging to this level is very small and at room temperature all excess electrons are moved to the conduction band. The conductivity of the n-doped semiconductor is larger than that of the intrinsic semiconductor. The procedure of inserting materials with a smaller number of valence electrons is called p-doping. In this case, there are some electrons missing to form the covalent bonds. A missing electron in the valence band is called a hole. The electrons of the covalent bonds can easily change their membership to a specific atom by filling the place of a hole. Thus, the holes can move nearly freely through the p-doped semiconductor material which increases the conductivity. The atoms of p-doping materials are called *acceptors*. The improved conductivity is the main reason for doping semiconductors.

If an n-doped and a p-doped part of a semiconductor are placed next to each other, the area of contact is called p-n junction. Due to the different concentrations of electrons and holes in both parts of the material, electrons diffuse to the n-doped part where they recombine with holes. The charged atoms cannot move and are responsible for the so-called *space-charge region*. An electric field forms. The electric field causes a drift which is directed opposite to the diffusion. The result is an equilibrium state. The area around the contact of p- and n- doped part is characterised by a largely reduced number of free charge carriers and therefore called *depletion zone*.

A p-n junction used as semiconductor device is called a diode. There are two ways of using a diode in electrical circuits: the *forward biased mode* and the *reverse biased mode*. Connecting the positive terminal of a power supply to the p-doped part of the semiconductor, the electrons in the p-doped part of the depletion zone can reach the positive pole and thus an electrical current flow is possible for voltages larger than the voltage which is needed to collapse the depleted region. Swapping the power supply terminal, the diode is operated in reverse bias mode. Electrons are injected in the p-doped part. They combine with holes and thus, the depletion zone increases. The larger the bias voltage, the larger gets the depletion zone. If the

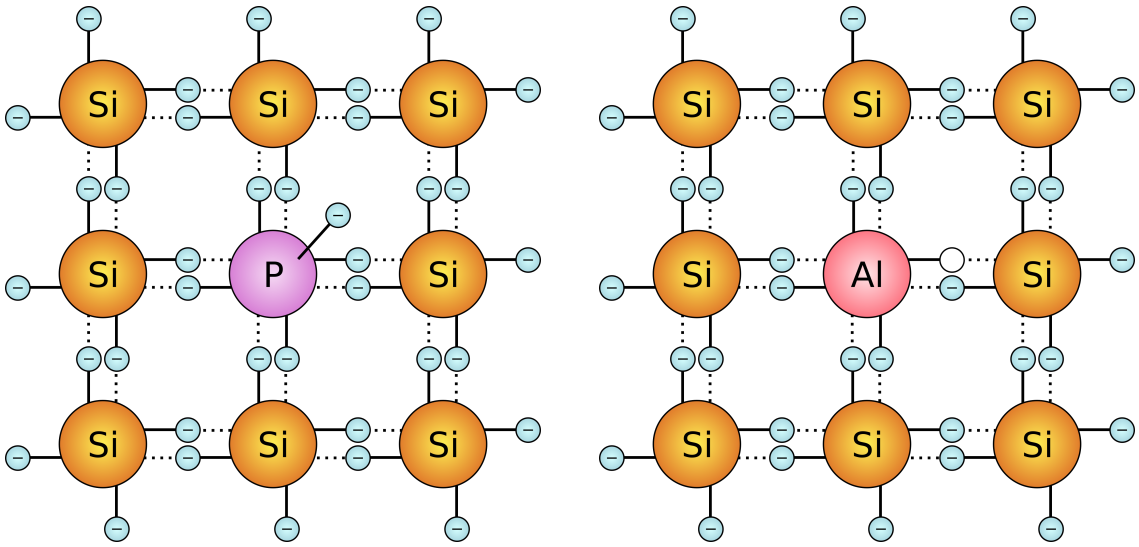

(a) n-doping [Hen10a] **(b)** p-doping [Hen10b]

Figure 3.2.: Schematic view of doping silicon. Silicon belongs to the fourth main group of the periodic table. Thus, it can be n-doped with materials from the fifth main group (for example phosphorus as in (a)) and p-doped with ones from the third main group (exemplary aluminum as depicted in (b)). n-doping leads to excess electrons while p-doping produces holes moving in opposite direction as electrons.

voltage is large enough to expand the depletion zone to the complete semiconductor material, the material is called fully depleted.

3.1.3. Silicon Strip Detectors

The working principle of diodes in reverse bias mode is the general principle of semiconductor particle detectors. Figure 3.3 depicts the geometry and working principle of silicon strip detectors. The sensor consists of a p-doped silicon bulk with implanted n^+-doped strips. The strips are arranged in parallel and are covered with a silicon dioxide (SiO_2) layer. The readout is performed AC-coupled via aluminum readout strips. The sensor back side is made of a thin p^+-doped layer and an aluminum layer for contacting the negative potential of the bias voltage.

Silicon strip detectors are operated in the reverse bias mode. Usually, the voltage is set to large enough values to fully deplete the sensor bulk. Thus, the number of free charge carriers due to thermal excitation is reduced to a minimum. A charged particle traversing the active sensor layer creates many electron-hole pairs. Due to the electric field in the depletion zone, the electrons drift to the n^+-doped strips while the holes move to the opposite direction. The drifting charge carriers induce a signal at the strips which is read out via the readout chip that is capacitively (AC) coupled to the strips. Due to separate readout of all strips, the position of the particle can be determined in one dimension.

Section 3.2 describes the interaction of particles with matter in more detail. Further information about silicon strip detectors can be found e.g. in [Har17].

3.2. Interaction of Particles with Matter

The interaction of particles with matter is essential for detecting particles. Since the interaction depends on the mass, charge and momentum of the incoming particle as well as the properties of

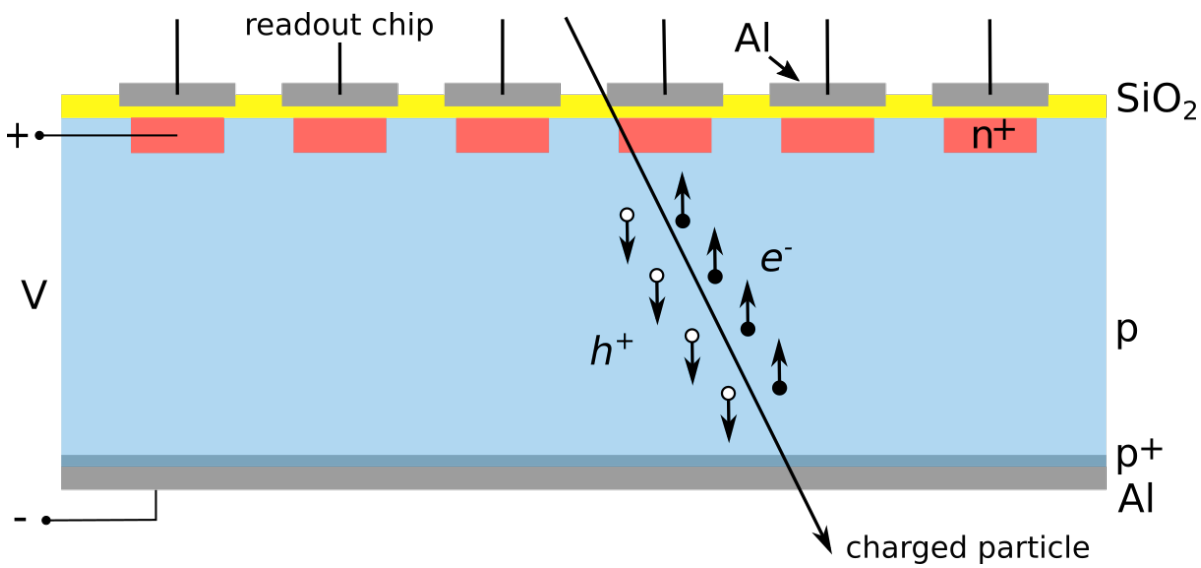

Figure 3.3.: Schematic view of the geometry and working principle of silicon strip sensors. Traversing the p-doped bulk, a charged particle creates electron hole pairs. Because of the reverse bias voltage and the resulting electric field, the electrons drift to the strongly n-doped strips. The induced charge can be read out AC-coupled. For that purpose, the strips are electrically insulated from the aluminum readout chips via a silicon dioxide (SiO_2) layer. The bottom side of the sensor is covered with a strongly p-doped layer and an aluminum layer allows contacting the negative bias voltage terminal. Adapted from [Dro18].

the target material, specialized sub-detectors are needed to measure specific particle properties as best as possible. Therefore, understanding the interaction is very important for the success of an experiment. The interaction with matter differs for charged and neutral particles and is explained in the following two sections. If not stated otherwise, the whole section is based on [Dem14].

3.2.1. Charged Particles

The mean energy loss per distance of *heavy charged particles* while traversing a material can be described by the *Bethe equation*

$$-\left\langle \frac{\mathrm{d}E}{\mathrm{d}x} \right\rangle = 4\pi N_A r_e^2 m_e^2 c^2 z^2 \frac{Z}{A}\frac{1}{\beta^2}\left[\frac{1}{2}\ln\left(\frac{2m_e c^2\beta^2\gamma^2 T_{\max}}{I^2}\right) - \beta^2 - \frac{\delta(\beta\gamma)}{2}\right]. \tag{3.1}$$

N_A	Avogadro constant	β	ratio of velocity to the speed of light
r_e	classical electron radius	γ	Lorentz factor
m_e	mass of the electron	$T_{\max}$	maximum kinetic energy transferred to the electron in a single collision
c	speed of light		
z	charge of the incident particle	I	mean excitation energy
Z	atomic number of the matter	$\delta(\beta\gamma)$	density effect correction
A	mass number of the matter		

Ionization is the main reason of energy loss for these particles. Equation (3.1) is valid for transverse momenta of $0.1 \lesssim \beta\gamma \lesssim 1000$ of the incident particle and intermediate-Z materials. For $\beta\gamma > 1000$, the radiative effects increase and dominate the energy loss while

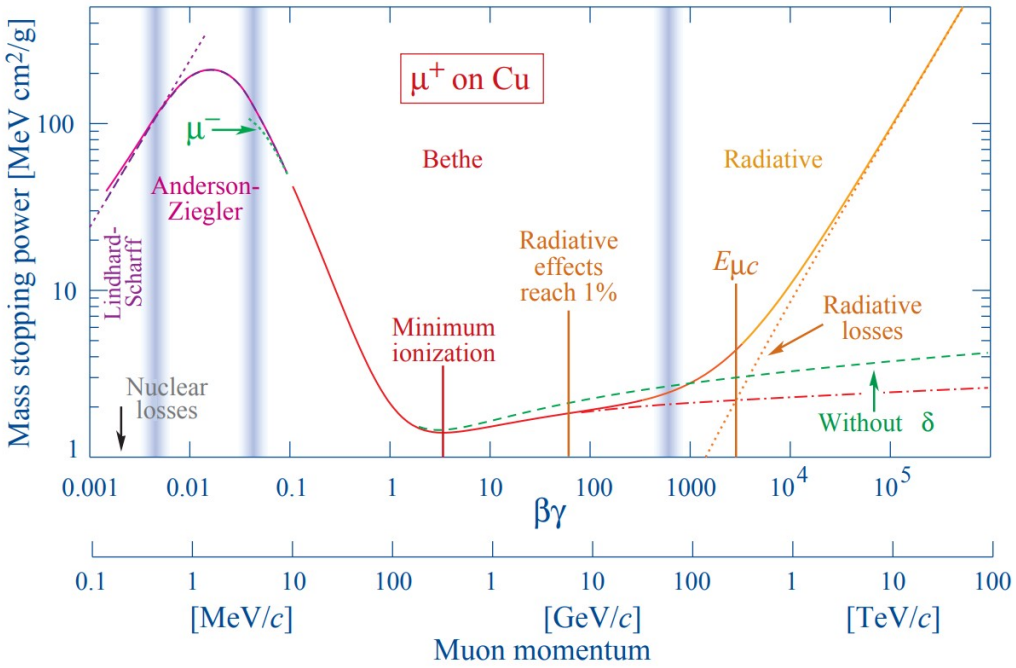

Figure 3.4.: Mean energy loss per distance of positive muons in copper. As a function of $\beta\gamma$ there are four areas of the mean energy loss of heavy charged particles in material. For low $\beta\gamma$, nuclear effects are important. Radiative effects are dominating for large $\beta\gamma$. The middle region ($0.1 \lesssim \beta\gamma \lesssim 1000$), where the minimum is located, can be described by the Bethe Equation (3.1). [Tan+18]

for $\beta\gamma < 0.1$ nuclear effects have to be taken into account. The mean energy loss has a minimum at around $\beta\gamma \approx 3$. Particles with minimum energy loss are called *minimum ionizing particles* (MIPs) and penetrate deeply into matter. Thus, the detection of MIPs with particle detectors has to be considered in the design requirements in particular. The mean energy loss per distance is exemplary shown for positive muons in copper in Figure 3.4. More detailed information can be found in [Tan+18].

The energy loss in matter of *light charged particles*, such as electrons or positrons, at particle energies lower than 10 MeV is dominated by ionization. Møller and Bhabha scattering as well as positron annihilation contribute only with a small part to the fractional energy loss per radiation length. For larger energies, the increased influence of the electromagnetic field of the nuclei leads to increased bremsstrahlung. The material dependent critical energy can be defined as the energy where the effect of bremsstrahlung and ionization are equal. The order of the critical energy is around $E_c = 10\,\text{MeV}$ [Tan+18].

3.2.2. Neutral Particles

There are three interaction processes of *photons* with material. The atomic photoelectric effect represents the main part of the total cross section for photon energies lower than 10 keV. The photon transfers all of its energy to an atomic electron. The photon is then absorbed and the atomic electron is ejected from the atom. For middle energies, Compton scattering dominates. The incoming photons scatter inelastically with the electrons of the matter by transferring parts of their energy to the electrons. At energies larger than two times the rest mass energy of an electron (1.022 MeV), electron-positron pair production in the nuclear field dominates the total cross section.

Neutral hadrons cannot be detected directly in a detector. They have to interact with the detector material via scattering to produce charged particles. Detailed information about the interaction of neutral particles, such as neutrons, can be found in [LR09].

3.3. 2S Modules for the CMS Phase-2 Outer Tracker

The CMS Phase-2 Outer Tracker will consist of 5616 PS modules and 7680 2S modules in total. As one of eight module production centers, the *Institute of Experimental Particle Physics* (ETP) at the *Karlsruhe Institute of Technology* (KIT) will build 1500 to 2000 2S modules. In the following, the module mechanics, electronics and readout will be introduced, before the arrangement of the 2S modules in the CMS Phase-2 Outer Tracker is described in Section 3.3.4. The 2S modules as well as the design of the whole CMS Phase-2 Outer Tracker are described in detail in [CMS17].

3.3.1. Module Mechanics

Figure 3.5 shows the exploded view of the 1.8 mm 2S module with its components. There is a second 2S module variant called 4 mm 2S module. The main difference is the width of the carbon fiber reinforced aluminum (Al-CF) spacers which are responsible for the sensor spacing. Other important tasks of the Al-CF spacers are constituting the main cooling part and fixating the module in the detector as supporting structure. Each sensor has two rows of 1016 strips, each approximately 5 cm long, resulting in an active area of 90 cm^2. The pitch of the strips is 90 µm. Both sensors are arranged parallel and back to back in the module.

The flexible *frontend hybrids* (FEH) are electrically connected to the sensor strips via wire bonds. On the *service hybrid* (SEH), the electronics for powering and optical readout are mounted. The SEH connects the two FEHs at one side of the module.

Within this thesis, two versions of 2S module prototypes are used for the measurements. The variants are called 8CBC3 prototype module and 2S prototype module. Photographies of both of them are shown in Figure 3.6. Mechanically, they differ by the dimensions of the FEHs and SEHs. The FEHs of the 8CBC3 prototype modules are wider due to so-called *Concentrator Integrated Circuit* (CIC) [Nod+18] extension mezzanines which allow to plug the CICs on the FEHs. In the 2S prototype version, this part is not required because the CIC is bump-bonded directly on the FEHs. The electronic components included in the 8CBC3 prototype modules are less space saving than that of the 2S prototype modules. Thus, the SEH is extended with a balcony housing the electronics. Both module prototypes should be mountable in the setup designed within this thesis.

For handling and reading out the modules in the readout station designed in [Kop18], they are mounted on aluminum carriers as visible in Figure 3.7. The carrier provides mechanical support and the modules top and bottom side is covered and thus protected with acrylic glass. Some measurements presented within this thesis are performed with modules mounted in the readout station. This is a temperature controllable setup for performing laboratory tests with 2S modules.

3.3.2. Module Electronics

The strip readout is performed by eight *CMS Binary Chips* (CBCs) per FEH. Each CBC is connected to 254 sensor strips. 127 of them belong to the upper sensor while the same number belongs to the lower sensor. The readout channels are connected alternating to both sensors. Thus, even channel numbers are connected to the strips of the lower sensor and odd channel

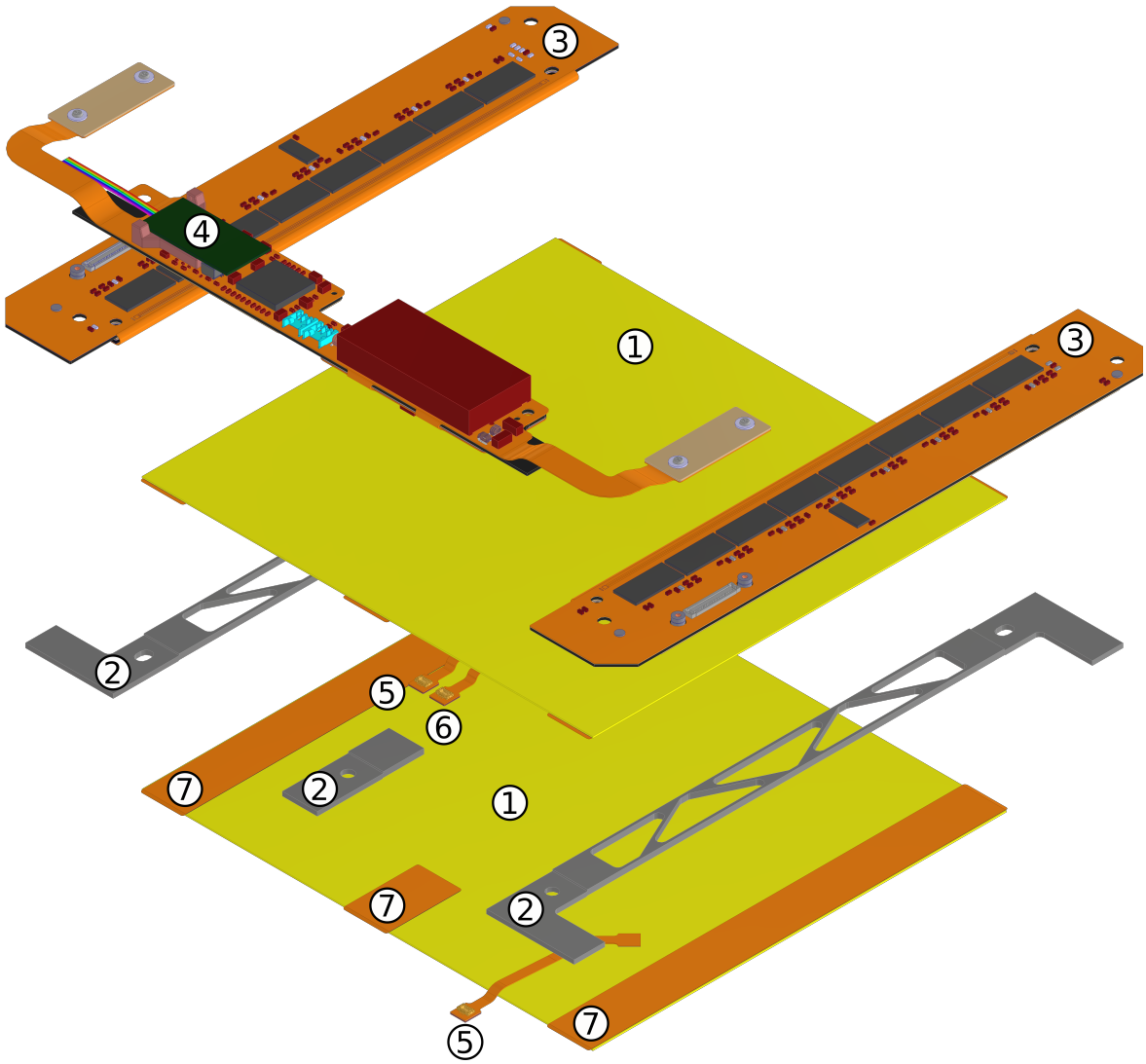

Figure 3.5.: Exploded view of the 1.8 mm 2S module variant. The different components of the 2S modules are: two silicon strip sensors (1), carbon fiber reinforced aluminum (Al-CF) spacers (2), two frontend hybrids (3), one service hybrid (4), high voltage tails (5), a temperature sensor (6) and strips of polyimide tape for electrical isolation (7). Similar to [CMS17].

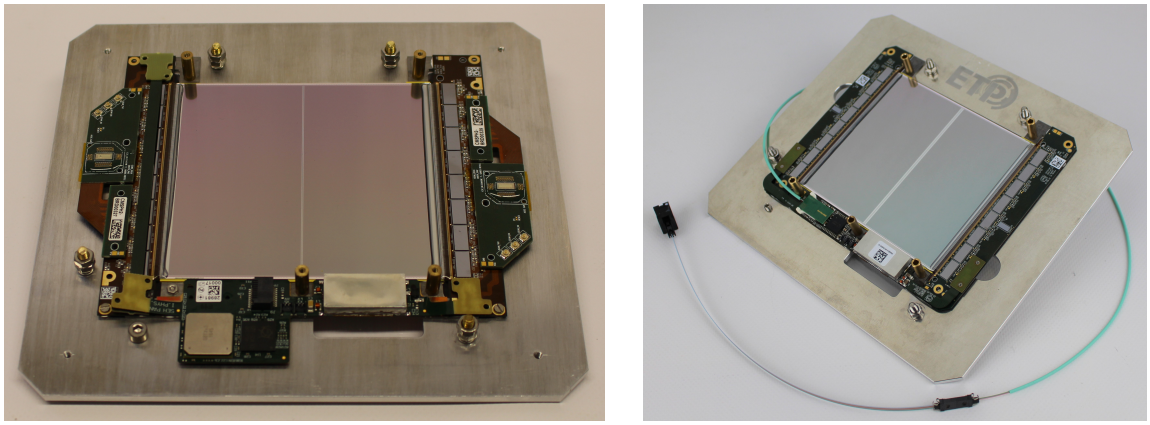

(a) 8CBC3 prototype module **(b)** 2S prototype module

Figure 3.6.: Picture of an 8CBC3 and 2S prototype module. The 8CBC3 prototype module depicted in (a) has a balcony on the SEH which prevents the mounting of such prototype modules on a TB2S ladder. Other differences to the 2S prototype modules shown in (b) are the CIC mezzanines on the FEHs and the right to left converter on the left FEH.

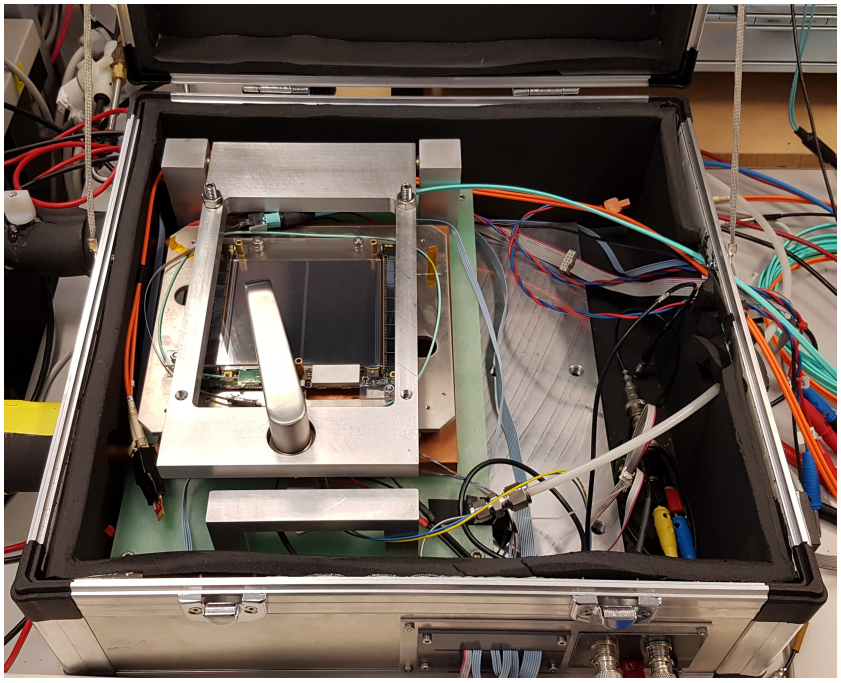

Figure 3.7.: The module readout station. A 2S prototype module is mounted on its carrier in the module readout station described in [Kop18]. It is a temperature controllable setup designed for laboratory tests with 2S modules.

numbers provide the readout of the upper sensor.[1] In total, the 16 CBCs of both FEHs are able to read out the 4064 strips of the module. The combined readout of both sensors allows the combination of hits to stubs as described in Section 2.3.2. Neighboring CBCs on a FEH are connected to each other to ensure the detection of stubs extending to the channels of two CBCs, resulting two data streams. The stub data contributes directly to the L1 trigger decision at 40 MHz while the trigger data is only sent out when a trigger is received from the back-end. The CBC is able to read out AC-coupled sensors and is designed for silicon sensors with p-type bulk. Detailed information about the CBC3 can be found in [Pry16b].

Test pulses can be injected directly into the channels' frontends to test if they are responsive. This is made with a charged capacitor. The amount of injected charge can be adjusted in Digital Analog Converter (DAC) counts. This internal threshold-unit can be expressed in units of electrons via

$$TPA_{\mathrm{e}^-} = \left(255 - \frac{TPA_{\mathrm{V_{CTH}}}}{\mathrm{V_{CTH}}}\right) \cdot 537\,\mathrm{e}^- \,. \tag{3.2}$$

[Pry16a; Bra13]

The larger the pulse height, the smaller is the injected amount of charge.

The low voltage power (LV) and high voltage bias (HV) are connected to the module on the SEH. The module is designed to tolerate a bias voltage up to 800 V while the leakage current is not expected to rise above the maximum leakage current of 2 mA per module after the radiation exposure of the module in the CMS experiment [CMS17]. The SEH is connected to the FEHs via two miniature connectors. It houses the DC-DC converter [Fel+17] which generates the necessary voltages for the ASICs[2] on the SEH and FEHs from the 10 V LV source. In case of the 8CBC3 prototype modules the data coming from the CIC on the FEH is serialized by the *gigabit transceiver* (GBTX) [Wyl+12] on the SEH. The optical data connection to the back-end is made by an optoelectronic transceiver, called VTRx. For the slow control of the ASICs on the module, an additional chip, called GBT-SCA [Car+15], is directly mounted beside the GBTX.

In the final 2S prototype modules, some electronic components are iterated to new more powerful and space-saving versions. The GBT-SCA and GBT are replaced by the *low power* upgrade of the *gigabit transceiver* (lpGBTX) ASIC [Kul+19]. The Versatile Transceiver (VTRx) is replaced by the VTRx+ [Tro+17].

3.3.3. Module Readout

For the module readout, the *Phase-2 Acquisition and Control Framework* (Ph2_ACF) [CMS21] is developed within the CMS Community. It is responsible for the communication with the processing and storage of data recorded by the 2S modules. All hardware components are embedded in the framework to be able to configure the hardware with the Ph2_ACF.

The FC7 evaluation board [Pes+15] is a µTCA[3] compatible Advanced Mezzanine Card (AMC) for data acquisition during the module testing in the research and development phase as well as during the production phase. It is compatible with the *FPGA*[4] *Mezzanine Card* (FMC) Standard. The FMC cards can e.g. enable the optical readout of the modules and provide the interface for external triggers such as from a scintillator signal.

The hardware development is continuous and the DAQ system needs to be adapted accordingly. Before taking data with a new software version, their functionality is tested. It provides the following tests as command line tool:

[1] The channel numbering starts at the first channel of CBC number zero with zero.
[2] Application-Specific Integrated Circuits
[3] Micro Telecommunications Computing Architecture
[4] Field Programmable Gate Array

Offset Calibration

To reach a uniform response of all CBC channels of a FEH, possible mismatches in the comparator and amplifier signal have to be equalized. This is possible via an 8-bit offset adjustment. The uniform response is achieved by scanning all threshold values and determine the threshold value with a hit occupancy of 50 %. This threshold is called the pedestal. Adjusting the offset of each CBC channel, the pedestals can be equalized to a FEH specific trim value.

Noise Scan

While changing the internal threshold in steps of $1\,\mathrm{V_{CTH}}$, the number of hits is counted. The noise is Gaussian distributed with its mean at a specific threshold-value called pedestal. The 2S module readout is binary which results in an increase of the number of hits per number of triggers, called hit occupancy, from zero to one proportional to the integral of the Gaussian function. Thus, the error function

$$F(x) = \frac{1}{2}\,\mathrm{erf}\left(\frac{x-y}{\sqrt{2}\sigma}\right) + c \tag{3.3}$$

is fitted to the occupancy to determine the pedestal value y at which the occupancy is 0.5 and the width σ. The width is referred to as noise. Measurements are performed at a specific threshold value in the range where the noise hit occupancy is nearly zero. In general, measurements are performed with threshold values at least five times the noise away from the pedestal.

Trigger Latency Scan

To take data, it is important to know the delay between the trigger signal and the time when the hits corresponding to this trigger can be read out. This time is called *hit latency* for the readout of single hits and *stub latency* in case of stubs. While performing a latency scan, the signal is read out at different clock cycles in a user defined latency range. The clock cycle at which the number of hits/stubs peaks is the hit/stub latency of the measured system.

Data Taking

After this steps, data can be taken at a user defined threshold and the hit and stub latency determined as described above. The data are stored by the Ph2_ACF in a raw data format. Additionally, the data taken for this thesis are stored in a ROOT tree [BR96].

3.3.4. Module Arrangement

In an ideal case, a solid angle of 4π should be covered by the CMS detector in order to detect as many particles as possible. Thus, the Inner and Outer Tracker have to be built as hermetically as possible. To prevent gaps between the module sensors, they have to overlap at all four edges with the sensors of the neighboring module. To ensure these requirements, the modules are arranged in different structures depending on the position in the Inner or Outer Tracker. Figure 2.4 shows the different parts of the Outer Tracker: the *Tracker Barrels* with PS (TBPS) and 2S modules (TB2S) are located in the central region while the *Tracker Endcap Double Discs* (TEDD) are the support structures of the tracker in the endcap regions.

The TBPS consists of three concentric layers with 2872 PS modules in total. Each concentric layer is divided into three parts. In the central region, the modules are arranged flat while they are tilted in the two more forward sections.

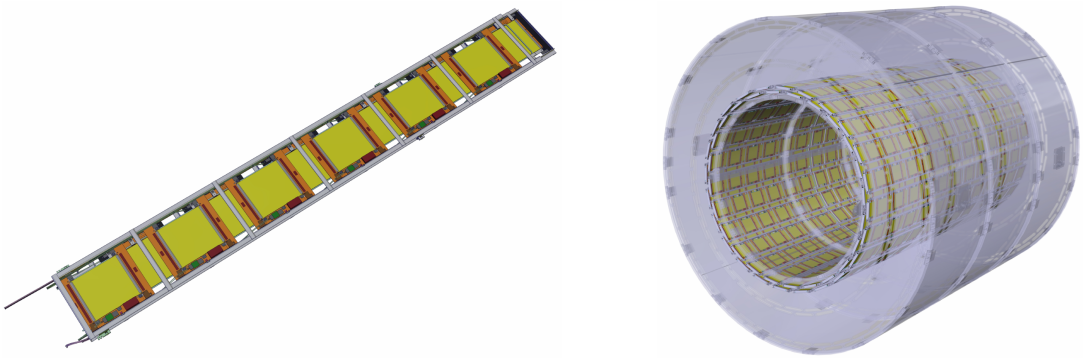

(a) Ladder [CMS17] **(b)** TB2S support wheel [CMS17]

Figure 3.8.: Ladder and TB2S support wheel. A fully assembled ladder equipped with twelve modules is depicted in (a). The innermost layer of the TB2S support wheel in (b) is equipped with assembled ladders.

In the TB2S 4464 detector modules will be mounted. The substructure of the TB2S part is the *ladder*. As visible in Figure 3.8(a), one ladder is equipped with twelve modules, overlapping in z-direction. In total, the TB2S consists of 372 ladders. They are mounted on a support wheel depicted in Figure 3.8(b). All ladders are staggered in φ-direction to ensure hermetic coverage. As the length of one ladder is equal to half the length of the barrel, the barrel is built of two ladders in z-direction, overlapping at $z = 0$.

The endcap part of the Outer Tracker is made of double-discs. Due to assembly reasons, the discs are split in half-discs or dees. One dee can be seen in Figure 3.9(a). Each disc is then compound of two dees and two discs form one double-disc. The innermost ten r-layers of one double-disc are equipped with PS modules while the outer five layers consist of 2S modules. Four double discs are then combined to a TEDD unit shown in Figure 3.9(b). There are two TEDD units in the CMS experiment, one at each detector side.

The local distance of the modules in the Outer Tracker is 4 mm inside a ladder and approximately 3 cm in between two neighboring ladders. To ensure that they do not influence each other, this thesis presents the conception of a setup to read out up to three modules at such close distances and to investigate their possible crosstalk in the readout mode. Further details about the 2S module arrangement in the CMS Phase-2 Outer Tracker can be found in [CMS17].

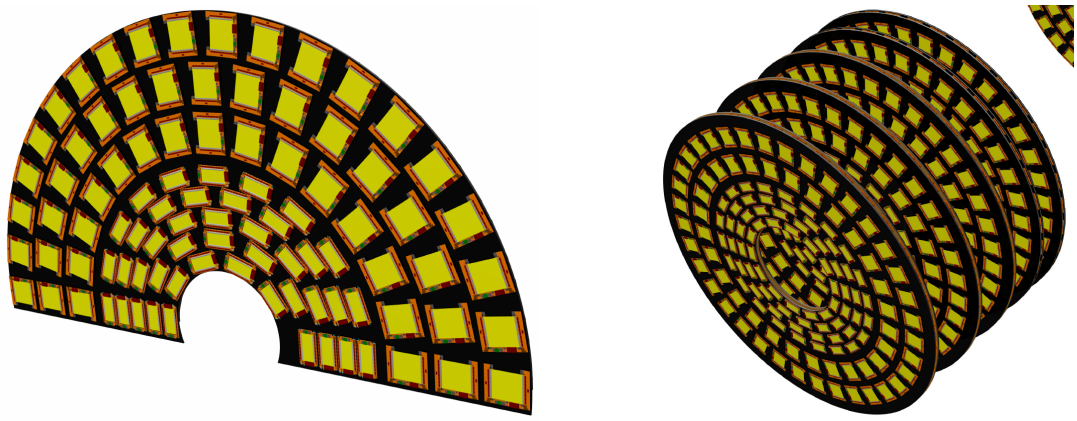

(a) Dee [CMS17] **(b)** TEDD unit [CMS17]

Figure 3.9.: Dee and TEDD unit. A fully assembled dee can be seen in (a). PS modules are mounted in the innermost five layers while 2S modules equip the outer layers. Four dees form a double disc which are arranged to TEDD units depicted in (b). One edge of the second TEDD unit of the CMS detector can be seen on the upper right side of the picture.

Part II.

Main

4
The 2S Muon Hodoscope

To prove the functionality of 2S modules as particle trackers, cosmic muons can be used. For that purpose, a 2S muon hodoscope with up to three module layers was designed. The hodoscope can be used for various studies such as the synchrony of the module readout as well as the muon signal charge and track reconstruction. Section 4.1 describes the experimental setup while Sections 4.2 and 4.3 give insights in measurements with one and three modules.

4.1. Experimental Setup

Figure 4.1 shows the muon hodoscope. It consists of a base plate and a cover plate of polyvinyl chloride (PVC) whereupon two scintillators can be placed. The setup allows to insert the individual modules on the carriers mentioned in Section 3.3.1. The modules can be oriented in two directions which are rotated by 90° with respect to each other. The topmost and lowermost sensor are spaced 6 cm apart in z-direction. The middle module is placed exactly in between. With the sensor distance of 1.65 mm, the z-distance between the nearest sensors of two neighboring modules is 2.75 cm.

The whole experimental setup of the 2S muon hodoscope is depicted in Figure 4.2. The hodoscope is placed in an aluminum box to shield the biased sensors from light. Each module has its own dry air flux directed to the DC-DC converter to avoid overheating. The raw signals from both scintillators are discriminated and put in coincidence. The coincidence signal is then converted from the *nuclear instrumentation module* (NIM) standard to the *transistor-transistor logic* (TTL) to serve as a trigger input for the module readout. The cosmic muon rate through the scintillator area can be estimated by a counter attached to the coincidence trigger signal.

For the measurements performed within this thesis, the strips of all the modules are oriented in the same direction. Thus, a two-dimensional tracking of muons will be possible. The bias voltage is set to $-300\,\mathrm{V}$.

4.1.1. Detector Acceptance

Due to the geometry of detector systems, particles with certain incidence angles are detected more likely than others. The parameters describing a two-dimensional detector system are the length L and the height h. The angle θ represents the incidence angle of the particle.

Particles traversing the detector vertically can be detected along the full length L, while the length is reduced to $L - \Delta x$ for particles with incidence angle $\theta \neq 0°$. The detector acceptance of a two-dimensional detector system is thus given by

$$A = \frac{L - \Delta x}{L} = \frac{L - h \cdot \tan(\theta)}{L} = 1 - \frac{h \cdot \tan(\theta)}{L}\,. \tag{4.1}$$

The maximal detectable angle is given by the value for which the detector acceptance is zero and can thus be calculated via

$$\theta_{\max} = \arctan\left(\frac{L}{h}\right)\,. \tag{4.2}$$

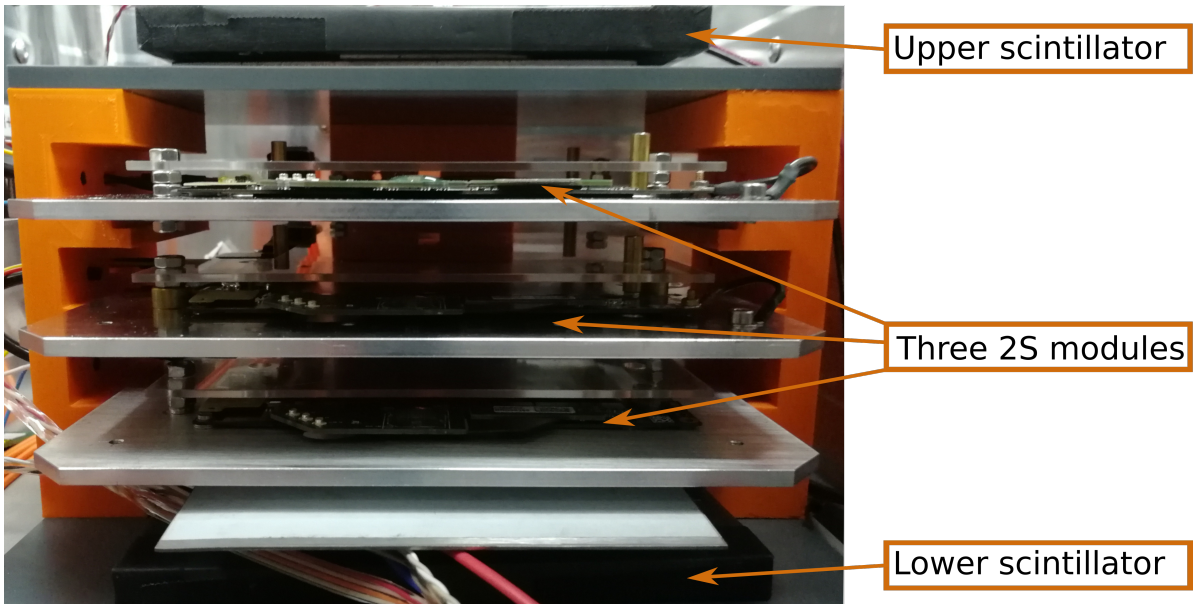

Figure 4.1.: 2S muon hodoscope. Up to three 2S modules can be placed onto their carriers in between the upper and the lower scintillator. The base and cover plate (gray) are made of PVC and the mechanical supports on the side (orange) are 3D-prints.

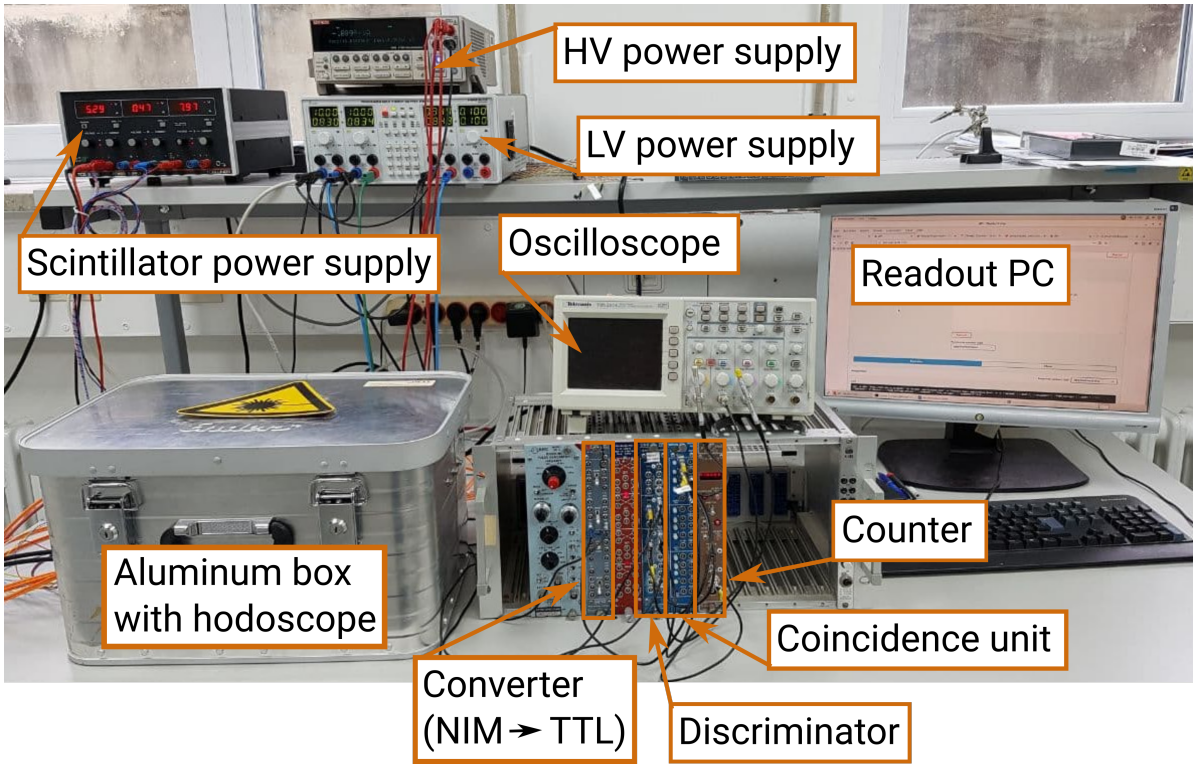

Figure 4.2.: Experimental setup of the 2S muon hodoscope. The 2S muon hodoscope is placed in an aluminum box which is flushed with dry air. The trigger signal of the scintillators is processed by a coincidence unit.

For the 2S muon hodoscope, the height $h = 13.7\,\text{cm}$ and length $L = 15\,\text{cm}$ are given by the vertical distance and the width of the scintillators. Thus, the maximal detectable angle is 47.6°.

4.1.2. Cosmic Muons

Cosmic muons are favored test particles in many laboratory experiments due to their availability and detectable charge unequal to zero. Even large detector systems at the LHC use trajectories of cosmic muons for alignment and calibration purposes.

In the earth's atmosphere at 15 km height, primary cosmic rays such as protons and small fractions of other nuclei collide with air molecules and cause showers of secondary particles. These secondary particle showers are dominated by pions (π^+, π^- and π^0). Charged pions decay weakly into muons and neutrinos ($\pi^+ \to \mu^+ + \nu_\mu$ and $\pi^- \to \mu^- + \overline{\nu}_\mu$). These muons are able to reach the earth's surface. On their way through the atmosphere they lose part of their energy by ionization. The mean energy of the muons at the ground is approximately 4 GeV. The angular distribution of muons at sea level is approximately given by

$$I(\theta) = I_0 \cdot \cos^2(\theta)\,, \tag{4.3}$$

where the flux at $\theta = 0°$ is given by $I_0 \approx 70\,\text{m}^{-2}\text{s}^{-1}\text{sr}^{-1}$. [Tan+18] With Equation (4.3) and the scintillator area of $A_{\text{scinti}} = 15\,\text{cm} \times 15\,\text{cm} = 225\,\text{cm}^2$, the expected cosmic muon rate of vertically incident muons is $1.57\,\text{s}^{-1}$.

4.2. Single Module Measurements

For an initial test of the detection technique and analysis procedure the first tests are made with a single module, called KIT_8CBC3_5. It is mounted in the 2S muon hodoscope and the scintillators are placed on the base and cover plate as illustrated in Figure 4.1. The first steps before taking data are, as described in Section 3.3.3, a noise scan and a scan of the trigger and stub latency. The results can be seen in Figure 4.3. With $6.35\,\text{V}_{\text{CTH}}$ for FE0 and $6.28\,\text{V}_{\text{CTH}}$ for FE1, the mean noise is comparable to the noise known from other module readout setups. The largest number of hits (stubs) is detected at a latency of 93 (10) clock cycles. Thus, the latency is set to 93 and the stub latency to 10 clock cycles for the following measurements. The pedestal lies at $600\,\text{V}_{\text{CTH}}$. The threshold for recording approximately 375,000 events over the course of 63 hours is set to $555\,\text{V}_{\text{CTH}}$, which corresponds to a distance of seven times the noise to the pedestal. This threshold is far enough from the pedestal to keep the number of Gaussian noise hits low enough for tracking the cosmic muons. The number of events at this recording time is compatible with the muon rate of $1.57\,\text{s}^{-1}$ mentioned in Section 4.1.2.

For each event, variables such as the event number, the bunch crossing ID, the TDC phase value and the channels with hits and stubs are stored. The stubs are stored with the position of the mean cluster position in one sensor layer (*stub position*) and the offset in strips to the mean cluster position in the other layer, called *stub bend*. These variables are used within the analysis described in the following Section 4.2.1.

4.2.1. Analysis Workflow

Before analyzing the data, some selection criteria are used to exclude corrupt events. Those events can be identified by the bunch crossing ID. This event variable is a number counted by the firmware. Each 25 ns it is increased by one. The bunch crossing ID is recorded separately for each FEH of the module and should be identical for both FEHs in one event. Subsequent events are expected to have different bunch crossing IDs.

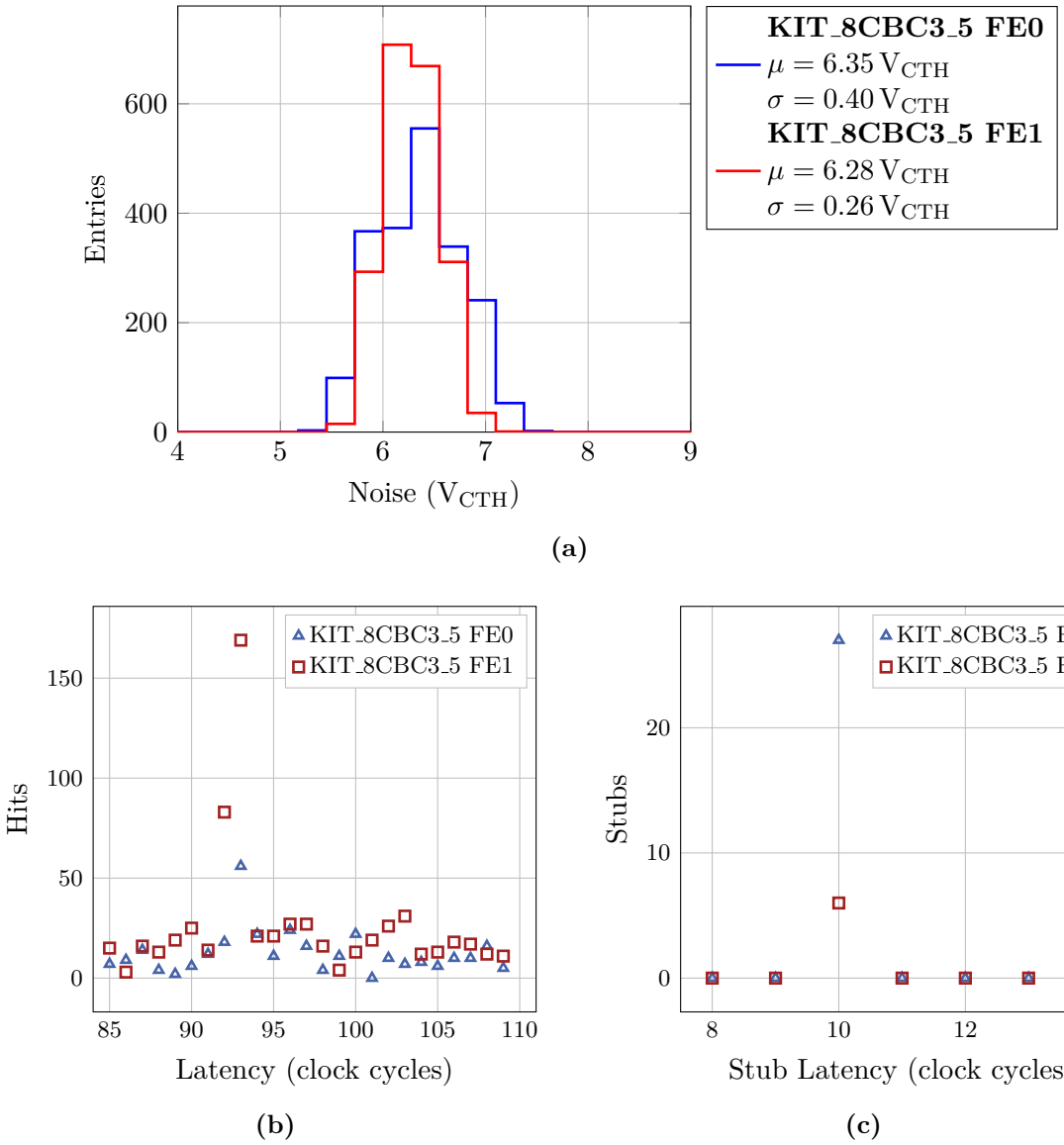

Figure 4.3.: Noise, latency and stub latency of KIT_8CBC3_5. The noise histograms are depicted in (a). The noise of both FEHs coincides. (b) shows the number of hits as a function of the latency in clock cycles while (c) depicts the stub latency. The peaks indicate the favored latency. It is set to 93 clock cycles for hits and to 10 clock cycles for stubs.

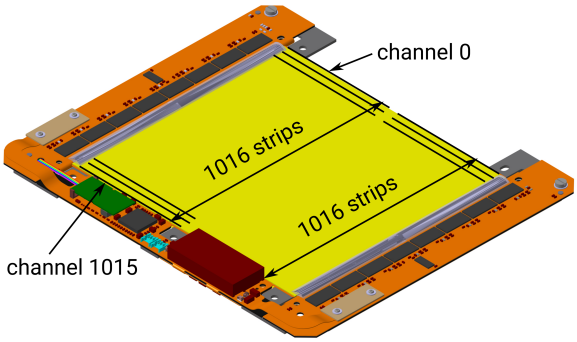

Figure 4.4.: Channel numbering. Within this analysis, the channel numbers start with 0 at the far side of the SEH and end with 1015 at the near side of the SEH.

However, in the data arise 328 events with different bunch crossing IDs between FEHs. This is equivalent to 0.08 % of all recorded events. Since this should not be the case when using the 2S modules in the CMS detector later, this issue was communicated to the firmware developers for further investigation.

Further events have to be excluded due to an additional phenomenon in which the same event is stored several times. If the bunch crossing ID of one event is the same as that of the previous event, the event is indicated as a double event and no longer considered in the following analysis. With 134,961 of 375,517 events, 33.45 % of all events are affected by this. This issue was also communicated to the software and firmware developers to fix the problem in later versions of the readout software Ph2_ACF.

During the analysis, the module hits per sensor and event are analyzed. As described in Section 3.3.2, even channel numbers belong to the lower sensor and odd channel numbers to the upper sensor. As depicted in Figure 4.4, the channel numbering used in this thesis starts with 0 at the far side of the SEH and ends with 1015 at the near side to the SEH. As a next step, the hits of the two FEHs are combined to hits belonging to the upper or lower sensor.

After the hits are assigned to the top and bottom sensor, clusters are searched in the hit data. A cluster is a combination of any number of hits in adjacent channels. It is described by the position of its center in units of half-integer strips and the cluster width in integer numbers of channels belonging to the cluster.

4.2.2. Simulation

To validate the data of the single module readout, a simulation of the expected results is performed. The general idea of the simulation is to generate tracks with varying incidence angles through the two sensor layers of a module. For that, different parameters are used, which are listed in Table 4.1. The incidence angle θ is distributed according to

$$\text{Counts}(\theta) \propto I(\theta) \cdot A \propto \cos^2(\theta) \cdot A\,. \tag{4.4}$$

A describes the detector acceptance given in Equation (4.1). The angular distribution of cosmic muons can be found in Equation (4.3).

The track of the particle through the sensor layers is then split into parts of 1 µm length, called tracklets. For each track, a random Landau-distributed value is drawn for the induced charge in all tracklets of this track. The parameters of the Landau distribution are taken from [Har17]. They are specified for 1 µm silicon silicon strip detectors and also listed in Table 4.1.

Table 4.1.: Input parameters of the signal simulation. The table presents the name and value of all input parameters of the signal simulation. The parameters are grouped in different categories according to their part in the measurement system.

Category	Name	Value
general	number of simulated tracks	100000
	input angle	$\propto \cos^2(\theta) \cdot A$
sensor	thickness	290 µm
	strip pitch	90 µm
	tracklet length	1 µm
	Landau μ	76 e^-
	Landau σ	10 e^-
	Landau max	500 e^-
	charge sharing parameter p	5
	sensor distance	1.65 mm
chip	conversion factor	varied, (156, 166, 176, 186 or 196) e^-/V_{CTH}
	noise	6.5 V_{CTH}
	threshold	45 V_{CTH}

The charge generated on individual strips is calculated from the tracklet charges with the charge sharing model

$$W_L = \frac{(1-x)^p}{(1-x)^p + x^p} \quad \text{and} \quad W_R = \frac{x^p}{(1-x)^p + x^p} \tag{4.5}$$

described in [Mai19]. Depending on the position x in the sensor, the charge sharing model splits the tracklet charge in two parts W_L and W_R and assigns them to the charge of the two nearest strips of the sensor. The parameter p is called the charge sharing parameter. To each strip charge, Gaussian noise is added. Within this simulation, a charge sharing parameter of $p = 5$ is used because [Mai19] determined this value as the best fit for the 2S modules.

Since the 2S module readout is binary, all the strip charges above a chip dependent threshold value are treated as signal contributions. For the simulation, the threshold value and noise level are needed in units of electrons e^-. They are determined in units of V_{CTH} from the calibration described in Section 3.3.3. Thus, a conversion factor is needed. The simulation is performed with various conversion factor values starting from 156 V_{CTH} in steps of 10 V_{CTH} and ending at 196 V_{CTH}. [Mai19] names a conversion factor of 156 V_{CTH} for the 2S module system.

Sections 4.2.3 and 4.2.4 compare the simulation with the measured data. This is done by generating results that are directly comparable to the readout data of the module measurements. This involves the cluster width in both sensor layers, the offset of clusters in strips between both sensors and the seed charge. The strip within a cluster with the largest amount of charge deposited is called the seed hit. Thus, the seed charge is the charge collected in the seed strip. Section 4.2.3 compares this value between the simulation and the measurement data of a threshold scan.

4.2.3. Threshold Scan

During the threshold scan, the threshold value is varied from 200 V_{CTH} to 575 V_{CTH} in steps of 5 V_{CTH}. The range from 540 V_{CTH} to 560 V_{CTH} around the nominal threshold of 555 V_{CTH} is scanned more closely in steps of 1 V_{CTH}. At each threshold, 10,000 to 20,000 events are recorded.

Events are selected according to the criteria described in Section 4.2.1. Then, a cut on the TDC phase is applied to the data. The *time to digital converter* (TDC) phase is a variable that divides each 25 ns clock cycle in eight equal time intervals. A cosmic muon traversing the scintillators produces a trigger signal. The arrival time of a muon passing the scintillators and thus the trigger signal is equally distributed within a clock cycle of 25 ns. Due to this fact, all TDC phase values corresponding to the trigger signal occur with the same probability. With the CBC readout mode used for this measurement, hits are detected if the signal is higher than the predefined threshold at the rising edge of a clock cycle. Since the signal shape is similar for each signal generated by a muon, the detection of hits depends on the TDC phase value of the trigger signal. Therefore, triggering at some TDC phase values has a higher probability of a hit detection than at others. The TDC phase value corresponding to the trigger signal is generated by the firmware and is stored for offline analysis. For the further analysis, only events with the three most likely TDC phase values 5, 6 or 7 are used.

Figure 4.5 shows the measured cluster occupancy

$$\text{Cluster occupancy} = \frac{\#\text{ of clusters}}{\#\text{ of triggers}} \tag{4.6}$$

and the integrated seed charge extracted from the simulation for different conversion factors. These physical quantities are compared because they are proportional to each other. The 2S module readout is binary, which means that all channels with a signal larger than a predefined threshold are read out and stored as hits. The absolute values of the signal are not stored. The clustering has the effect that a cluster can be interpreted as the seed hit. Thus, the cluster occupancy is proportional to the integrated simulated seed charge. Comparing the data with the simulation by eye, a conversion factor of $176\,\mathrm{e}^-/\mathrm{V_{CTH}}$ fits the data best. The cluster occupancy at low threshold values is increased due to noise hits. Thus, the data points with a cluster occupancy larger than 0.6 are excluded from the fit. Due to this result, the simulation with the conversion factor $c = 176\,\mathrm{e}^-/\mathrm{V_{CTH}}$ is used for comparison with the data in the next Section 4.2.4.

4.2.4. Measurements at Fixed Threshold

The aim of the analysis of the measurements at fixed threshold is to search for tracks of cosmic muons traversing the active sensor layer of the module. Since cosmic muons traverse the sensor layer in one straight line, one cluster in each sensor layer is expected. The probability of two muons in one event is small enough to not consider this case. Thus, for tracking only events with just one cluster per sensor are considered for the further analysis. The percentages of the described event categories are listed in Table 4.2. Some events are stored without any hits. The active area of the modules 2S sensor is approximately $A_{\mathrm{2S}} = 2 \times 5\,\mathrm{cm} \times 1016 \times 90\,\mu\mathrm{m} = 91.44\,\mathrm{cm}^2$, while the scintillator area is approximately $A_{\mathrm{scinti}} = 15\,\mathrm{cm} \times 15\,\mathrm{cm} = 225\,\mathrm{cm}^2$. Due to the fact that the scintillators' active area is larger than the active area of the 2S sensors, more trigger signals are generated than there are reconstructable muon tracks. For vertically incident muons, the expected number of events with exactly one cluster per sensor is $A_{\mathrm{2S}}/A_{\mathrm{scinti}} = 0.41$ while 59.36 % of the events are expected to be empty. Thus, the recorded empty amount of 58.43 % meets the expectation for vertical muons. Since the incidence angle distribution is maximal for vertical muons, this is comparable in first order.

The cluster size of events with exactly one cluster per sensor is plotted in Figure 4.6 for both sensors. The expectation is that the cluster size increases with the incidence angle because the traveled distance of the muons within the sensor material increases. Since the muon angle distribution is maximal for angles around 0°, small cluster sizes are dominant. The measured

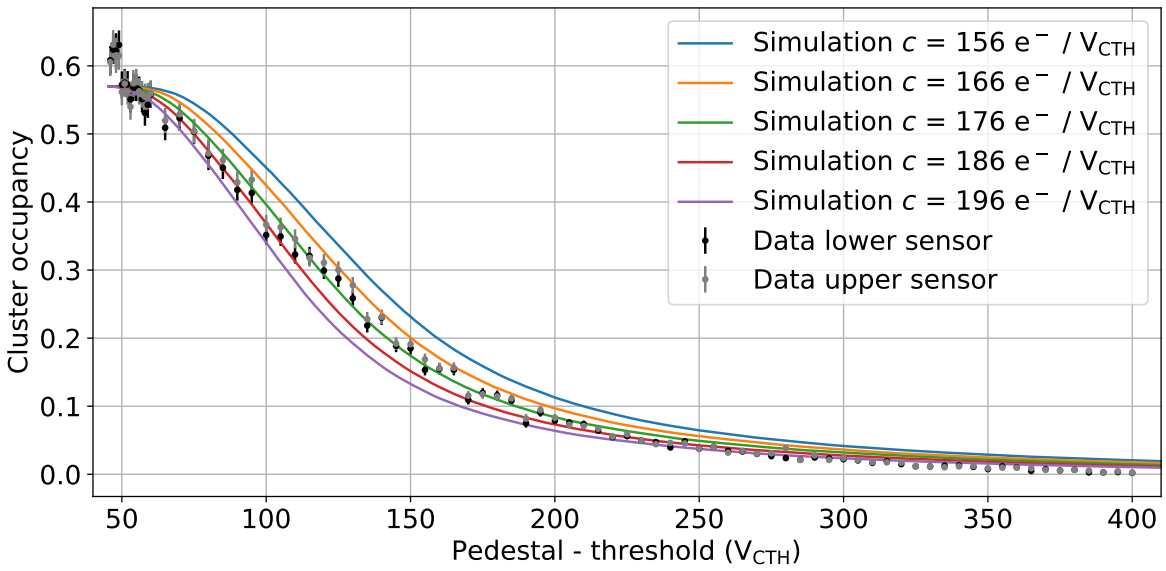

Figure 4.5.: Comparison between the measured cluster occupancy and the integrated simulated seed charge. The data fit the simulation well for a conversion factor of 176 e^-/V_{CTH}. The data points with a cluster occupancy larger than 0.6 are excluded from this fit by eye because noise hits cause this increase in the cluster occupancy. The data error bars are given by the error propagation of the statistical uncertainties of the number of clusters and triggers.

Table 4.2.: Selection criteria of the single module measurements. Event categories of the analysis with corresponding number of events and percentages of all events after the exclusion of double recorded events (240,556 events).

Event category	Number	Percentage
exactly one cluster per sensor	80,462	33.45 %
without any hit	140,561	58.43 %
more than one cluster in at least one sensor or zero hits in one sensor	19,533	8.12 %

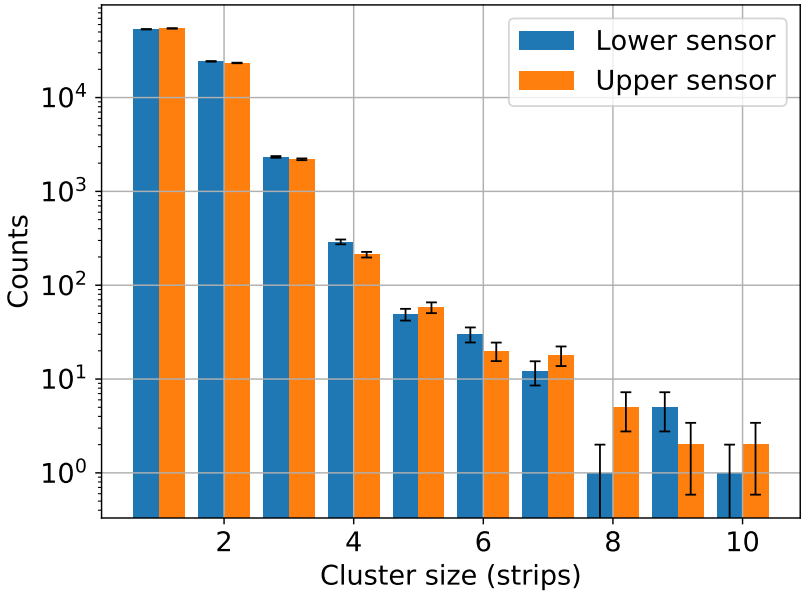

Figure 4.6.: Cluster size distribution. The histogram shows the number N of clusters as a function of the cluster size. The number of counts decreases with increasing cluster size and is equally distributed for both sensors. The maximum cluster size is 10 strips. The uncertainties are given by $\sqrt{N}$.

distribution in Figure 4.6 confirms this expectation. As expected, small cluster sizes appear more often than big cluster sizes. The maximum cluster size is 10 strips.

For the events with exactly one cluster per sensor, the offset in strips between the two clusters in the upper and lower sensor is calculated. In Figure 4.7, different offset values are histogrammed. The binning is chosen such that integer and half-integer offset sizes can be differentiated apart. As illustrated in Figure 4.8, other values are not possible. The same cluster size in both sensors leads to an integer offset as does any other even difference in cluster size. In contrast, a cluster size difference equal to an odd integer number always leads to half-integer offsets. Since the track of one muon is a straight line, the track length through the sensor is nearly the same for both sensors. Due to this fact, the same cluster size in both sensors and thus integer offsets of clusters are favored. This effect is observed in the data and confirmed by the simulation results. However, the data histogram overshoots the simulation for integer offsets while it undershoots the simulation for half-integer offsets. The data distribution of half-integer offsets has two maxima at about ± 5.5 strips. A larger offset in strips is correlated with a larger trajectory of the muon in the silicon sensor. Thus, it is more probable that the two clusters differ by an odd integer number, which results in half-integer offsets. The maxima of the simulated half-integer distribution are at ± 4.5 strips. The maximum detected offset is given by 22 strips. This corresponds to an incident angle $\theta \approx 47.7°$ which is equal to the expectation of θ_{max} mentioned in Section 4.1.1.

Figure 4.9 shows the average cluster size in strips versus the offset in strips for the recorded and simulated data. Two features of the plot attract attention: The average cluster size increases with increasing offset. This corresponds to the expectation that larger offsets respectively larger muon incidence angles are characterized by a longer trajectory of the muons through the sensor material. For small offsets, the average cluster size differs for integer and half-integer offsets. The average cluster size of half-integer offsets is approximately 1.5 strips whereas the average cluster size for integer strip offsets is 1 for zero offset and increasing the larger the offset is.

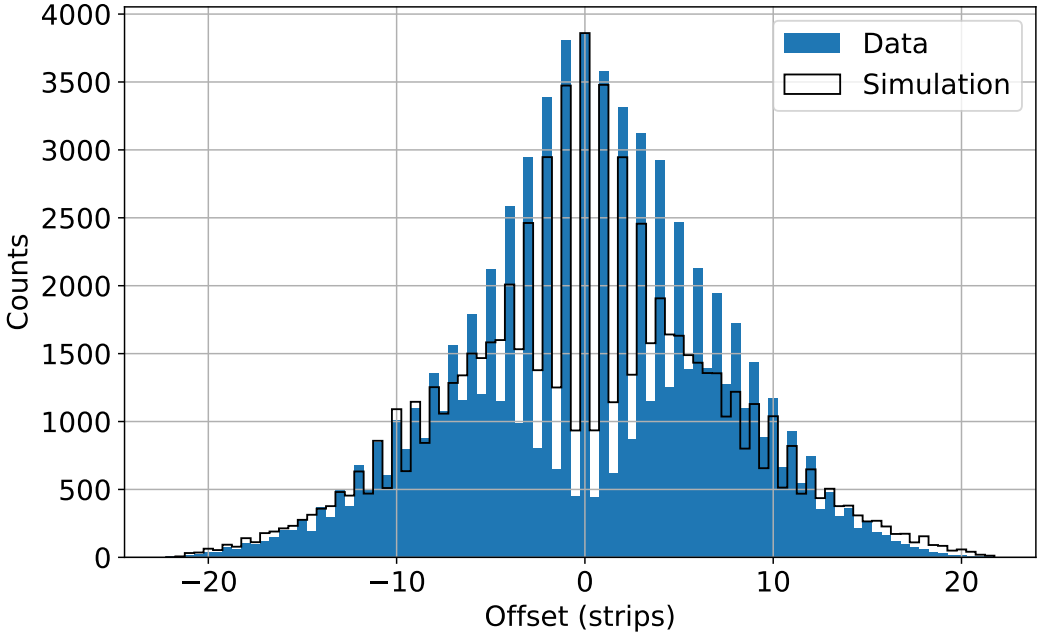

Figure 4.7.: Cluster offset distribution. The plot shows the cluster offset distribution of measured and simulated data. The number of counts decreases with increasing offsets. Integer values are favored with respect to half-integer offsets in strips. The number of counts in data overshoots the simulation for integer offsets while it undershoots it for half-integer offsets.

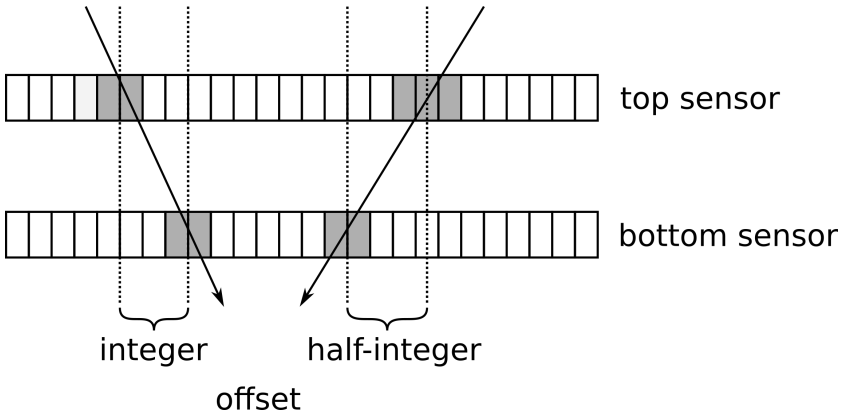

Figure 4.8.: Illustration of possible offset values. Only integer and half-integer offset values in strips are possible. If the cluster size in both sensors differs by an even number the offset in strips is an integer value. An odd difference of the cluster size leads to half-integer offsets in strips.

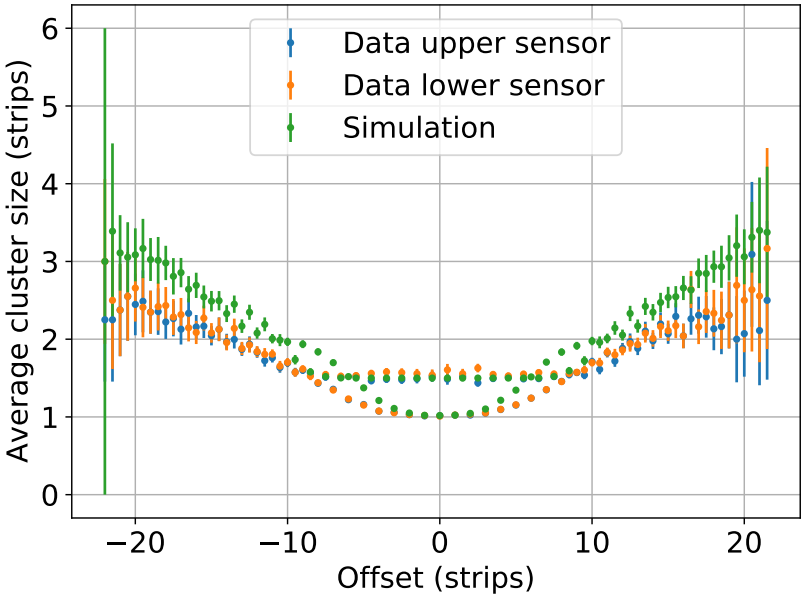

Figure 4.9.: Dependency of the average cluster size of the offset. The plot depicts the average cluster size in strips versus the offset in strips. As expected, the average cluster size increases with the offset in strips and is equally distributed for the upper and lower sensor. The error bars result from the error propagation of the statistical uncertainty of the counts per offset.

Let n_u denote the cluster size of the upper sensor and n_l the cluster size of the lower sensor. The cluster combination resulting in the smallest average cluster size 1 is given by $n_\mathrm{u} = 1$ and $n_\mathrm{l} = 1$. This combination is responsible for the minimum at 1 for integer offsets in strips. The combination $n_\mathrm{u/l} = 1$ and $n_\mathrm{l/u} = 2$ corresponds to the minimum at 1.5 for half-integer offsets. The combination of two clusters with one strip each leads to an average cluster size of one which explains the minimum for integer offsets at 1. Except for small half-integer-offsets, the simulated average cluster size is larger than the average cluster size recorded in the data.

4.3. Measurements with Three Modules

For the measurements with three modules, the 8CBC3 prototype modules called KIT_8CBC3_1, KIT_8CBC3_5 and KIT_8CBC3_6, are mounted in the hodoscope. The mentioned order corresponds to the mounting in the setup from bottom to top.

To perform measurements with three modules mounted in the hodoscope, they have to be read out synchronously. For that purpose, a dedicated version of the readout software Ph2_ACF is used. The measurements performed within this thesis are one of the first times that 8CBC3 module prototypes are read out synchronously. Thus, the dedicated software and firmware are not yet tested as much as other software versions. Possible problems during the module readout have to be communicated to the software developers.

As first steps, a noise scan and scans of the trigger and stub latency are performed. The results are depicted in Figure 4.10. For the measurements at a fixed threshold, a threshold of 555 $\mathrm{V_{CTH}}$ is used. With a pedestal of 600 $\mathrm{V_{CTH}}$ and a mean noise of 6.57 $\mathrm{V_{CTH}}$ this threshold value is seven times the noise above the pedestal. About 945,000 events are recorded over the course of 170 hours at this threshold in total. This is compatible with the muon rate of 1.57 $\mathrm{s^{-1}}$ mentioned in Section 4.1.2.

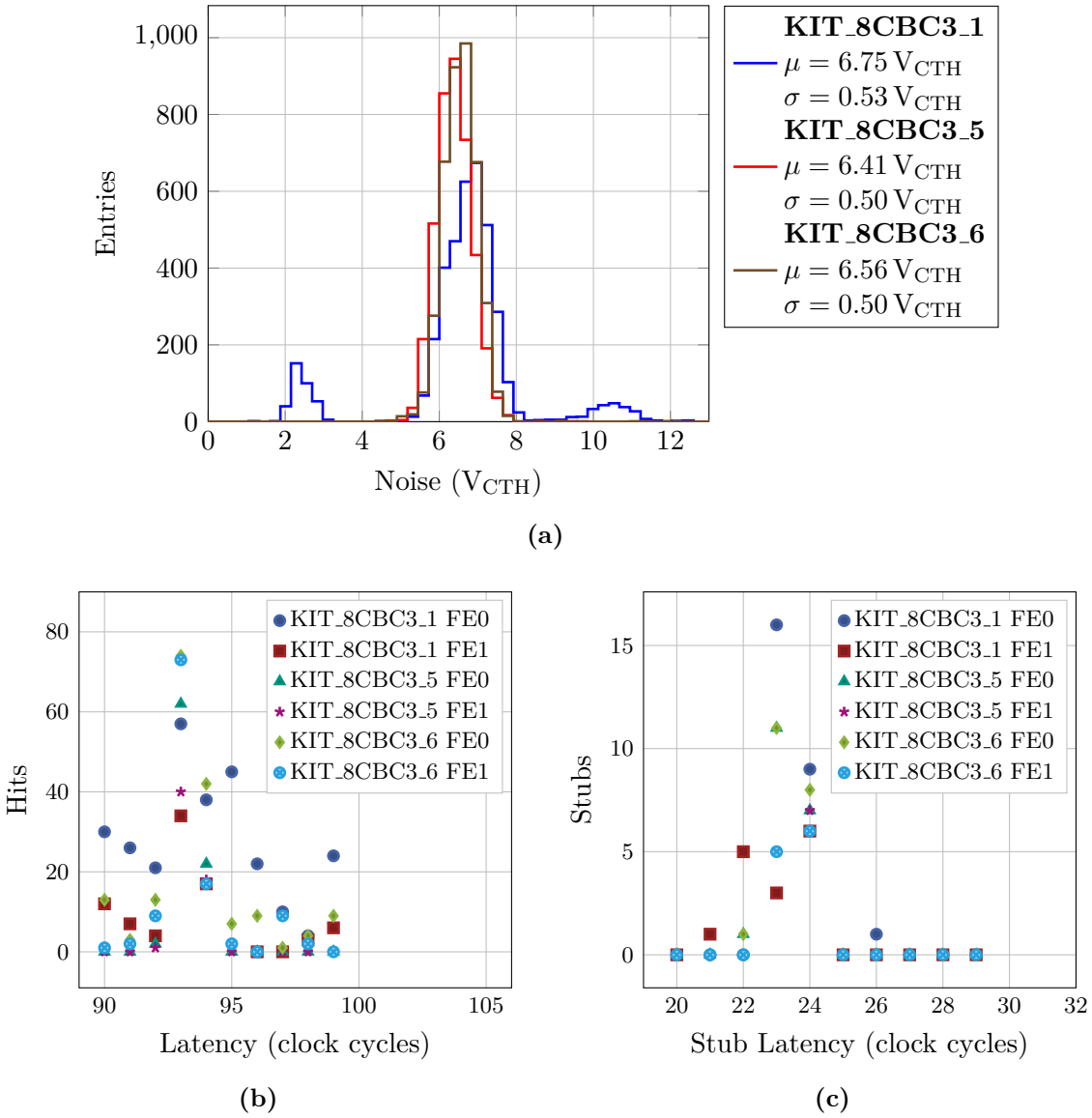

Figure 4.10.: Noise, latency and stub latency of KIT_8CBC3_1, KIT_8CBC3_5 and KIT_8CBC3_6 mounted in the 2S muon hodoscope. The noise histograms are depicted in (a). The noise level of all modules is nearly the same. The left additional peak of module KIT_8CBC3_1 results from unconnected strips while the right additional peak is resulting from some strips of the double length 10 cm. (b) shows the number of hits over the latency in clock cycles while (c) depicts the stub latency. The peaks indicate the favored latency. It is set to 93 clock cycles for hits and to 24 clock cycles for stubs.

4.3.1. Analysis Workflow

The phenomenon of double-stored events also appears in the three module measurement. With 186,494 events, 19.73 % of all events are affected. They are excluded in the following analysis. Also, there are 7525 events with a different bunch crossing ID stored for at least one FEH. With 0.80 % of all events, this readout bug occurred seldom but more often than in the case of one module (see Section 4.2.1).

The remaining 758,601 events are used for the further analysis which is described in the following step by step.

Masking

Noisy channels with a largely increased number of hits compared with the number of hits in the other channels, are masked in the further analysis. 25 channels of KIT_8CBC3_1 and four channels of KIT_8CBC3_6 are affected. No channels of KIT_8CBC3_5 have to be masked. Since this module is used for the single module measurements, no channels had been masked in the analysis of the single module measurements.

Alignment

To determine the relative module alignment in the hodoscope, the top and bottom module positions are considered fixed. Then, it is possible to determine the relative alignment of the two sensors in the middle module. The sensors alignment is performed individually. This procedure has to be repeated after each hardware change. For each alignment process 25,000 events are used.

The events with at least one hit in all sensors and fewer than eleven hits per sensor are used to align the middle module. This selection criterion is applied to the hits because it is expected that tracks from muons produce at most as many hits as it is observed in Section 4.2.4 and depicted in Figure 4.6. Due to common mode noise events with many hits per sensor, this selection criterion is necessary.

With the remaining events, tracks through the upper and lower module are reconstructed. For that purpose, the cluster positions are converted from units of strips to global coordinates in units of millimeters. With the selection criteria, it is possible to have more than one cluster per sensor. For all cluster combinations of the two upper and lower sensors, linear fits are performed. The track is reconstructed as the fit with the smallest χ^2. The track is then used to calculate the local displacement of the nearest cluster in the middle modules sensors to the penetration point of the track through the other two modules. If χ^2 is larger than 10, this track is not taken into account for the alignment because the physics motivated model of a straight muon track is not described by the data in this case.

The displacements are filled in a histogram, which can be seen exemplary for one alignment process and both middle modules sensors in Figure 4.11. The mean is calculated with a Gaussian fit to the histogram and is also depicted in Figure 4.11. For the tracking described in the next subsection, these mean displacement values are used to shift the hits of the sensors of the middle module. The difference of the two means is 27 µm, which can be interpreted as the misalignment of the modules sensors. The metrology measurements of this module give a displacement of (5 ± 10) µm. The results of the alignment do not lie within the uncertainty range. A reason could be that the 3D-printed mechanical side supports are not of the same height due to the production process of 3D-printing. A height difference of 2 mm between the left and right side leads to the measured sensor displacement of 27 µm. Considering this possible uncertainty of the setup, the alignment results are reasonable but this measurement is not able to determine the absolute value of the module's sensor displacement.

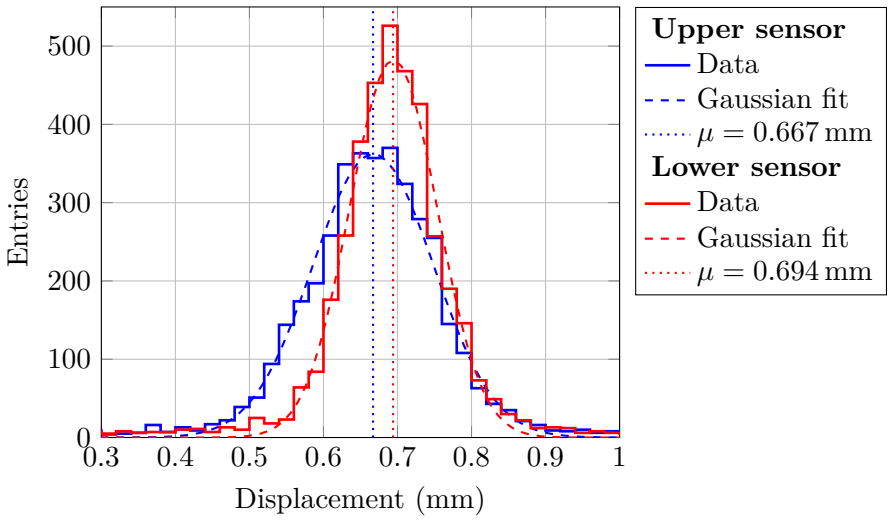

Figure 4.11.: Alignment. The histograms show the displacements of the upper and lower sensor of the middle module with respect to the tracks fitted through the other two modules. The mean of the Gaussian fit to the displacement histograms is depicted as well.

Table 4.3.: Selection criteria of the measurements with three modules. Event categories of the analysis with number of events belonging to each category and percentages of all events without the double recorded ones (758,601 events).

Event category	Number	Percentage
events with tracks	165,000	21.75 %
without any hit	294,757	38.86 %
more than ten hits in at least one sensor or zero hits in at least one sensor	298,844	39.39 %

Tracking

The tracking procedure is performed for all events with at least one hit in each layer but fever than 11 hits per sensor. The motivation for these selection criteria is to exclude noisy events with large number of hits and to filter events with tracks resulting from muons traversing all sensor layers. Tracks are reconstructed by a linear fit to all cluster combinations. The combination with the smallest value of χ^2 which fulfills the criterion $\chi^2 \leq 10$ is taken as a track. In total, 165,000 tracks are reconstructed from the data. This corresponds to 21.75 % of the selected events. The event numbers are summarized in Table 4.3

4.3.2. Measurements at Fixed Threshold

The angular distribution shown in Figure 4.12 is extracted from the data as described in Section 4.3.1. The incidence angle θ of the muon is calculated from the slope b of the linear regression as $\arctan(1/b)$. The basic shape is as expected: maximal at small angles and sloping symmetrically to zero for increasing as well as decreasing angles. The maximal detected angle of 54° is larger than the expectation of 47.6° calculated in Section 4.1.1. An explanation for this issue could be the fact that in principle, muons with an angle up to $\theta_{\text{max}} = 56.73°$ can be detected with three modules. This value results from the sensor width of approximately 9 cm

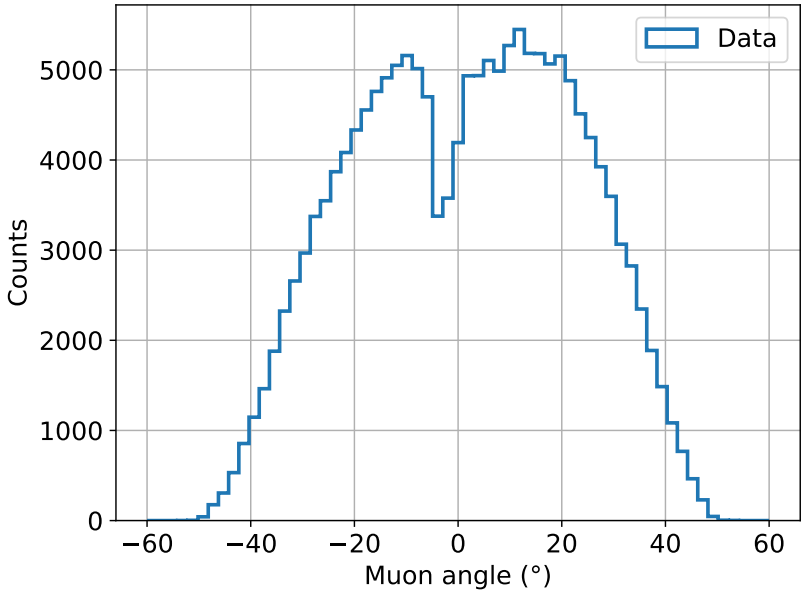

Figure 4.12.: Angular distribution of cosmic muons measured with three modules. The plot depicts the angular distribution of cosmic muons measured with three 8CBC3 prototype modules. The basic shape of the histogram is maximal around 0° and sloping down to zero until the maximal angle of 54° as expected from cosmic muons. The dip at small negative angles is unexpected.

and the distance of 6 cm between the furthest sensors of the hodoscope. If the scintillators were shifted relative to each other slightly, larger angles in one direction get possible. If the scintillators were shifted after some hardware changes in opposite direction, this could be the reason for this issue. The dip at small negative angles is unexpected and could result from the readout software problems described in the previous paragraph. They were communicated to the software developers.

The correlation plots of the undermost sensor, referred to as sensor 0, to one other sensor of each module are shown in Figure 4.13. The correlation and thus the tracks from the muons can be seen. The further the distance of the modules, the broader is the correlation. In Figure 4.13(c), bright spots in the diagonal can be seen. They correspond to nearly vertical muon tracks and are related to the dip in the angular distribution. The reduced number of vertical tracks can also be seen in Figure 4.13(a). The yellow diagonal with a large number of hits is interrupted but should be a continuous line. The reduced number of correlated hits (bright spots) is tested with different combinations of software and firmware. Taking data with the software version used for the measurements with a single module (see Section 4.2) leads to correlation plots without this phenomenon in the case of read out with the dedicated firmware as well as with the firmware of the three module Ph2_ACF version. It can be reasoned that the three-module readout software has a bug which has been communicated to the software developers.

Summing up, measurements of cosmic muons are possible with 2S modules. The muon charge signal and muon tracks are reconstructed with one single module mounted in the setup. The tracking of cosmic muons is also possible with three modules read out synchronously. However, problems with the readout software occurred during synchronous module readout. A description of the problems has been communicated to the Ph2_ACF developers.

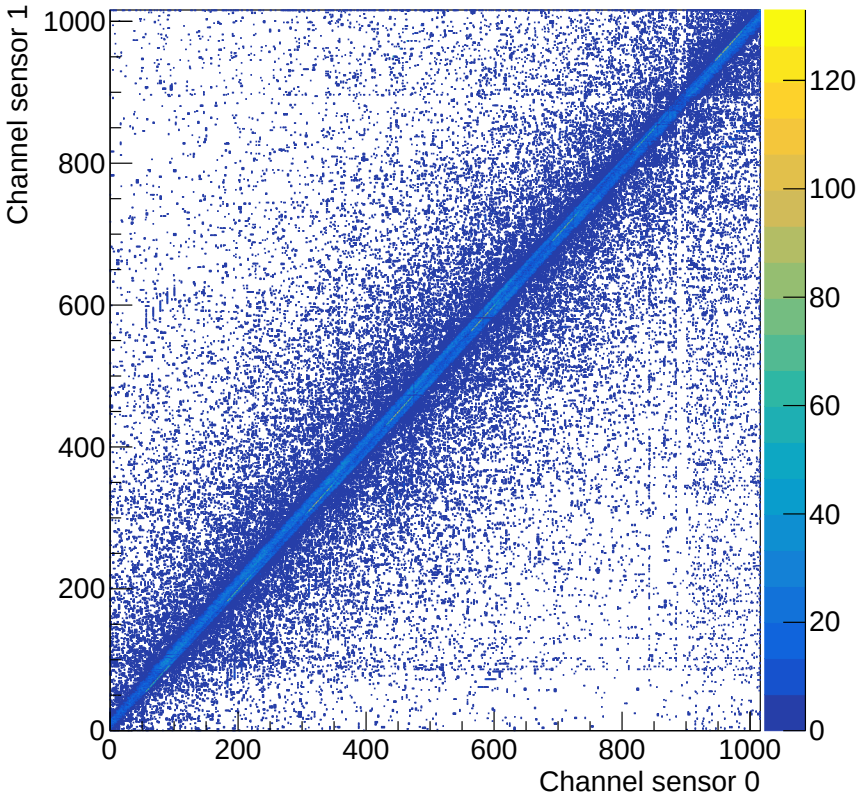

(a) Undermost module

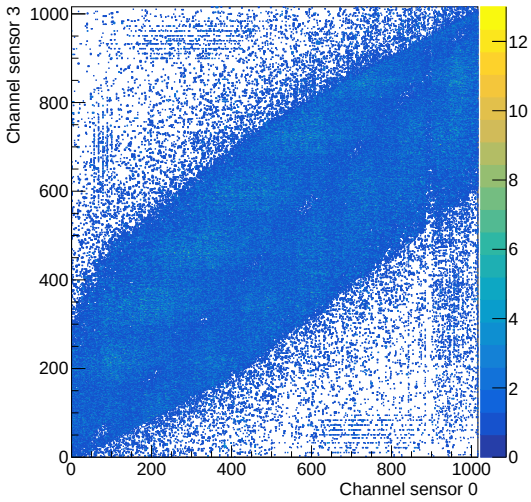

(b) Middle module

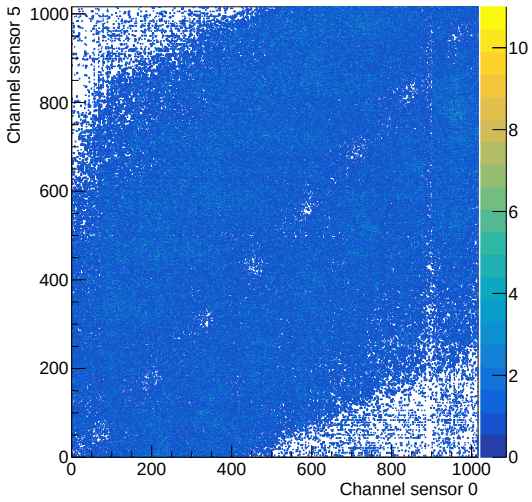

(c) Uppermost module

Figure 4.13.: Correlation plots. The plots depict the correlation of the undermost sensor 0 to three other sensors. Sensor 1 (a) belongs to the same module as sensor 0 while sensor 3 (b) and 5 (c) belong to the other two modules. As expected, a larger sensor distance leads to broader correlation. The bright spots on the diagonal represent the missing tracks near 0°.

5

The KArlsruhe LAdder MOckup (KALAMO)

Active electronic devices at close distances can influence each other. Thus, the electronic components on 2S modules such as the DC-DC converter could change the measurement results of 2S modules placed at close distances as it is done in the CMS Phase-2 Outer Tracker. To identify if there is crosstalk between modules read out synchronously and to locate the crucial components, the *KArlsruhe LAdder MOckup* (KALAMO) was designed within this thesis. Section 5.1 introduces the basic concepts and ideas of KALAMO, while Section 5.2 describes the experimental setup in detail. Section 5.3 presents the grounding studies performed with KALAMO while Section 5.4 summarizes test pulse studies.

5.1. Basic Concepts

The idea of KALAMO is to simulate the situation of the module placement and readout in the CMS Phase-2 Outer Tracker. For the design of KALAMO, the following points are considered as requirements:

- Studying the possible crosstalk between 2S modules shall be possible with up to three modules.
- With the setup, it shall be possible to simulate the readout with three modules inside a ladder and in between two neighboring ladders. For that purpose, two modules are mounted as in one ladder and the third one is mounted at the distance of the neighboring ladder.
- The 8CBC3 and 2S prototype modules as described in Section 3.3.1 are expected to be mountable in KALAMO.
- To perform grounding studies, the two sides of the ladder shall be designed isolated from each other. Thus, the electrical connection is provided only through the FEHs or can be added externally if required.

5.2. Experimental Setup

The designed parts are explained separately for the setup which simulates the situation inside a ladder and the one which simulates the situation in between two neighboring ladders. Both setups are placed on the same polyvinyl chloride (PVC) baseplate to isolate them from the ground of the aluminum box.

5.2.1. Ladder Configuration

A photography of one produced part of the setup can be seen in Figure 5.1. The ladder structure (for further details have a look at Section 3.3.4) is built of two aluminum bars that

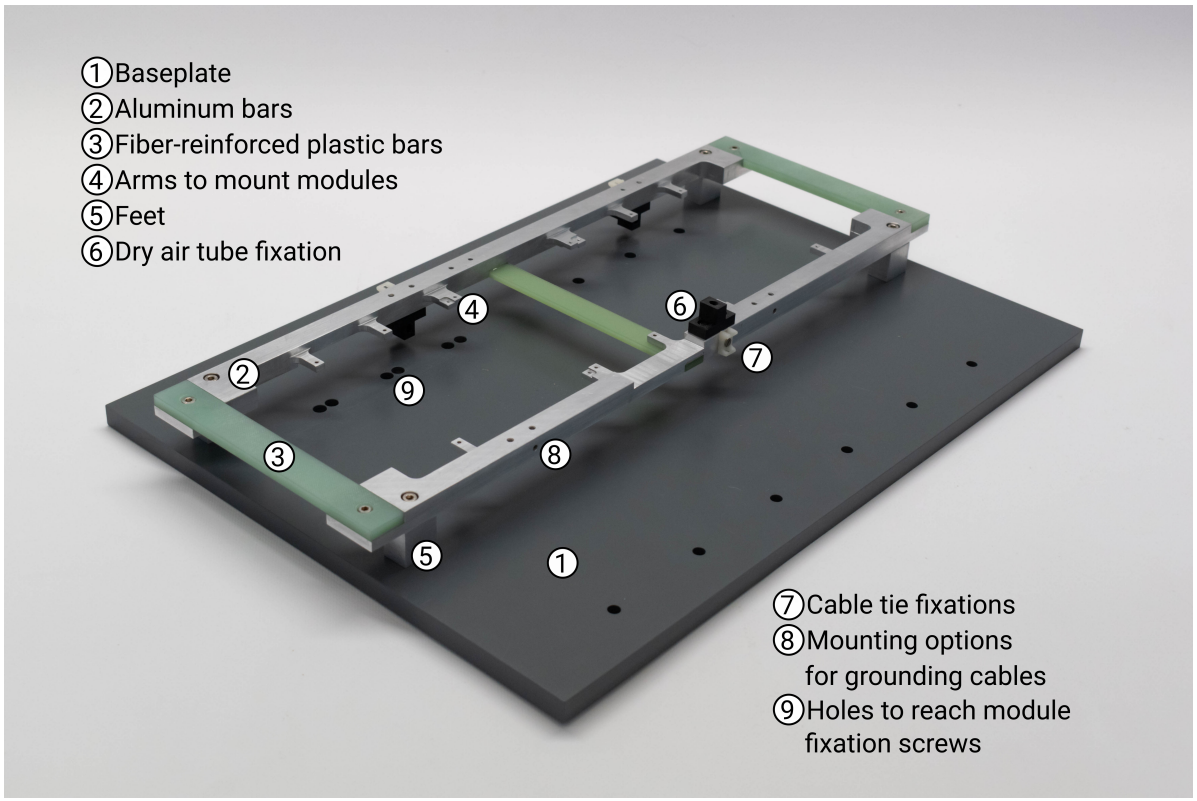

Figure 5.1.: Designed parts of the KALAMO ladder configuration. The frame to simulate the module readout inside a ladder consists of two aluminum bars connected via glass-fiber reinforced plastic bars.

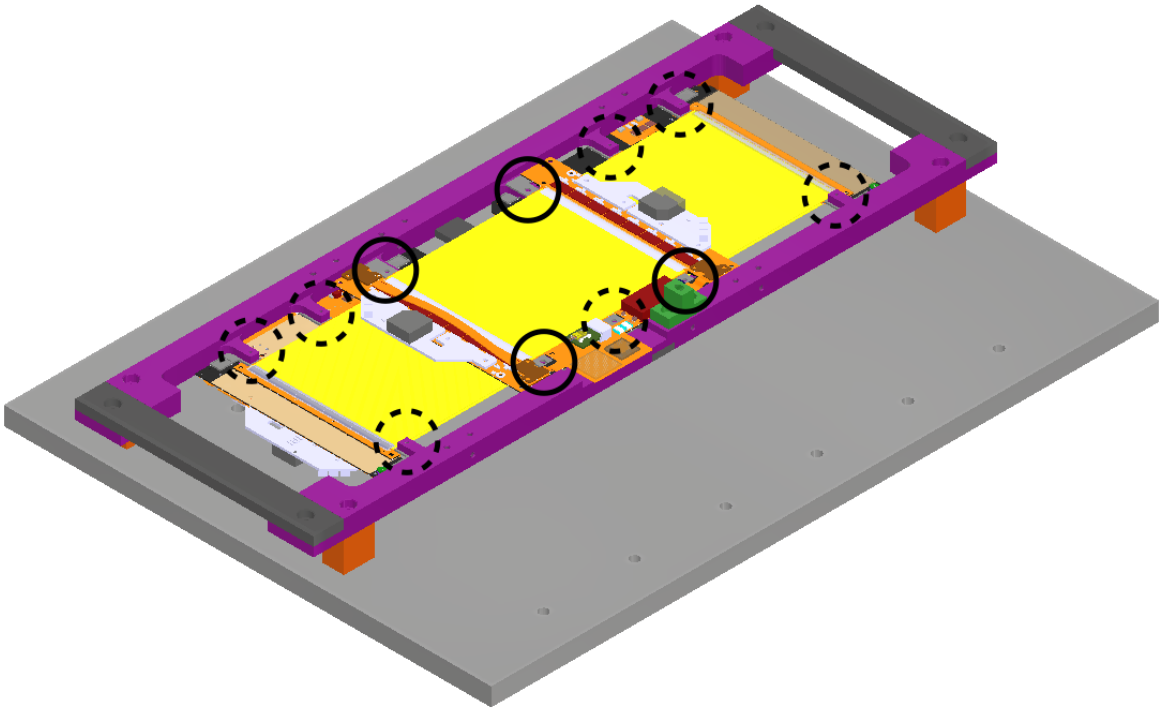

Figure 5.2.: Module arrangement of the modules mounted in the KALAMO ladder. Two modules are positioned facing downwards while the third module is oriented upright. Some mounting arms fixate two modules (continuous circles) from opposite sides and others enable the mounting of one module (dashed circles).

are connected via glass-fiber reinforced plastic bars. This ensures the electrical isolation of the aluminum bars. The modules can be mounted with screws on small arms analog to the mounting of the modules on the ladder structure described in Section 3.3.4. As viewable in Figure 5.2, some mounting arms are used for the mounting of two modules from opposite sides while others are used for the mounting of just one module. Inside a ladder, the distance of two neighboring modules is not always the same. They vary within a range of one centimeter. Thus, two ladder frames are designed to realize two different distances of the modules. Both frames differ just in the position of the threaded holes for the mounting of one module. Figure 5.3 illustrates this. At the small arms on which one module of each side is mounted, cavities are needed to leave space for parts of the FEH (see Figure 5.3(c)). To avoid twisting the modules while screwing them on the frame, the height of the mounting arms must not differ more than approximately 10 µm. This is only given when the frame is screwed on the feet. Thus, the frame has to be fixed on the legs before tightening the module mounting screws. Holes in the baseplate at the position of the module screws allow this sequence of mounting. At the position of the SEH balcony, the frame is thinner to leave space for it.

Black 3D-prints are responsible for the dry air tube fixation and cable tie fixations facilitate the cable management. Threaded holes are distributed all over the ladder frame to allow the mounting of grounding cables from the modules to the frame or the frame to the ground of the power supplies.

5.2.2. Barrel Configuration

The designed parts of the setup to read out up to three modules in a situation as in between two neighboring ladders are shown in Figure 5.4. Two modules are mounted in the ladder frame.

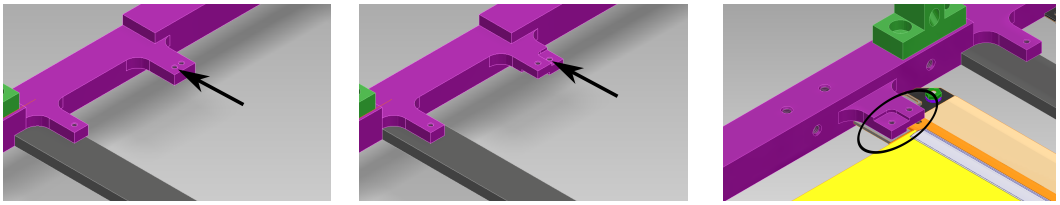

(a) Smaller module distance **(b)** Larger module distance **(c)** Cavity for FEH structure

Figure 5.3.: Arms for module mounting on the ladder frame of KALAMO. The positions of the threaded holes of the frame indicated with arrows depicted in (a) and (b) differ by 8 mm. Thus, the mounting of the modules with two different module distances is possible. As visible in (c) within the ellipse, the cavities in the small arms for module fixation leave space for some SEH structures of the module on the opposite side.

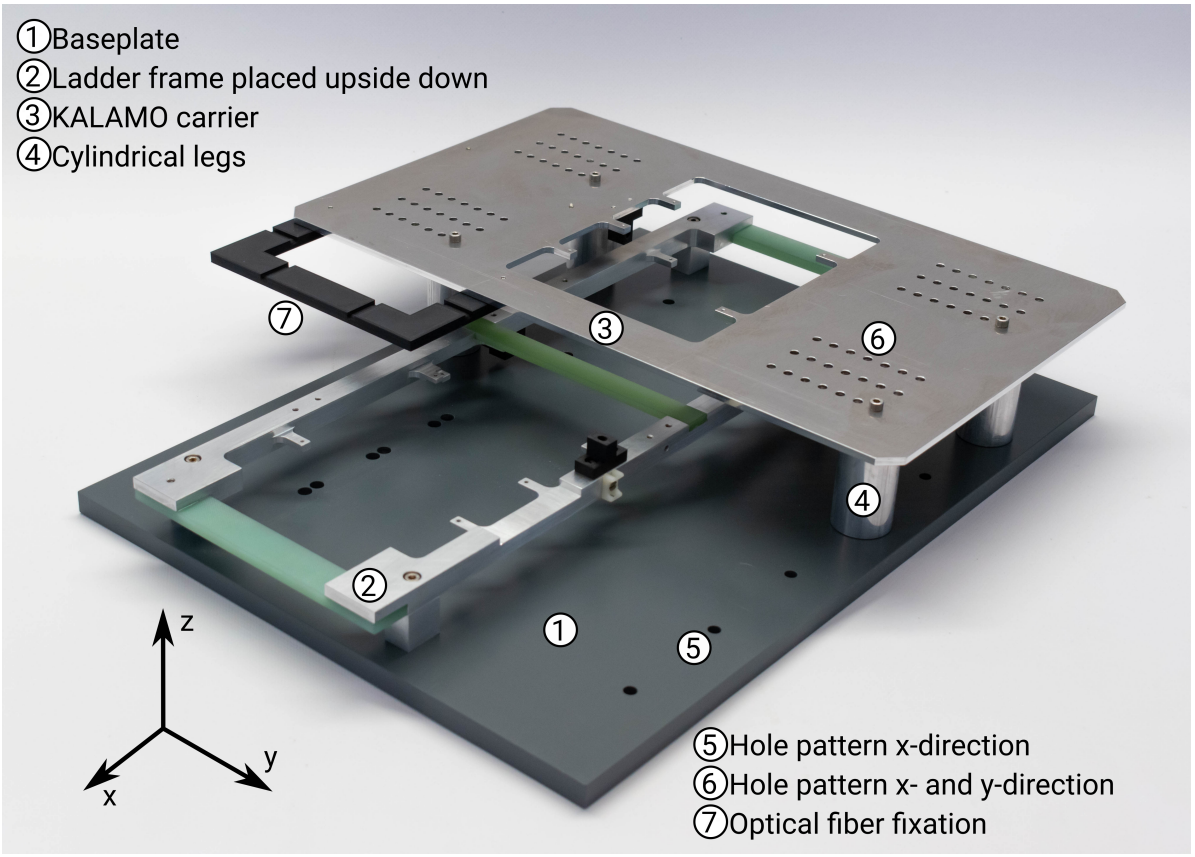

Figure 5.4.: Designed parts of the KALAMO barrel configuration. The setup to simulate the situation in between two neighboring ladders consists of the ladder frame depicted in Figure 5.1 and an additional carrier to mount one module upside down. The position of the upper module can be changed in x- and y-direction via hole patterns in the baseplate and the KALAMO carrier.

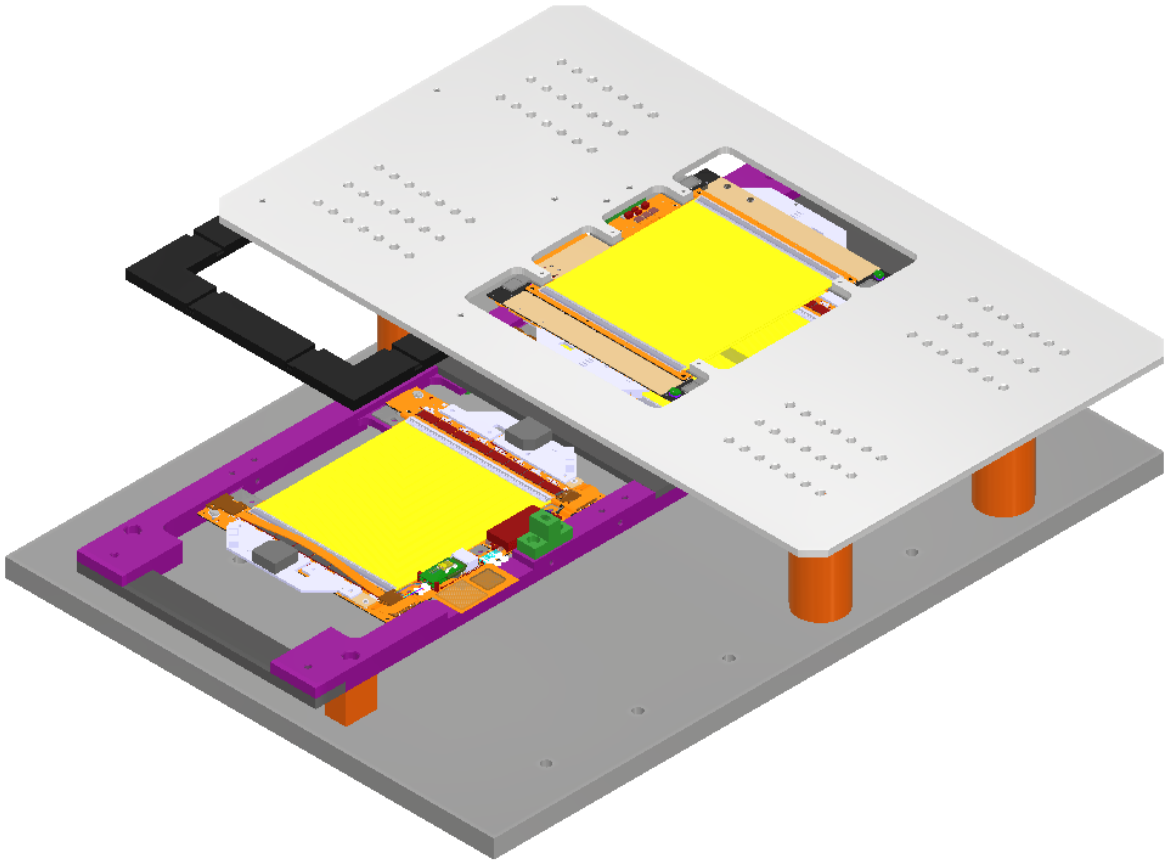

Figure 5.5.: Module arrangement of the modules mounted in the KALAMO barrel configuration. Two modules are mounted on the KALAMO ladder facing upwards. The third module is mounted on the KALAMO carrier facing downwards.

In contrast to the setup described previously, the ladder frame is placed upside down. Thus, the two modules face upwards. The third module is mounted on the large aluminum carrier, called KALAMO carrier, and is mounted facing downwards. This configuration of the modules is depicted in Figure 5.5. The carrier is placed on cylindrical legs and fixated with screws. A hole pattern allows a displacement of the upper module step by step with respect to the others. The position of the cylindrical legs can be changed via a hole pattern in the baseplate in steps of 6 cm in x-direction. Smaller steps of 2 cm are possible with the hole pattern in the large carrier. The movement of the upper module with respect to the others in y-direction is possible in centimeter steps with the hole pattern in the large carrier.

A black 3D-print ensures the safe management of the optical fiber. It ensures that the fiber is not in contact with the sensors of the lower modules. The carrier also contains fixations for cable ties and a dry air tube.

5.2.3. Laboratory Setup

The laboratory setup is similar to that of the muon hodoscope described in Section 4.1 and depicted in Figure 4.2. A high voltage power supply provides the bias voltage of the 2S sensors and the voltage for the readout electronics is provided by a four-channel power supply. For the readout of the modules, an FC7 board is used. The FC7 board is equipped with an FMC card which communicates with the modules. The FC7 board is connected with the local network

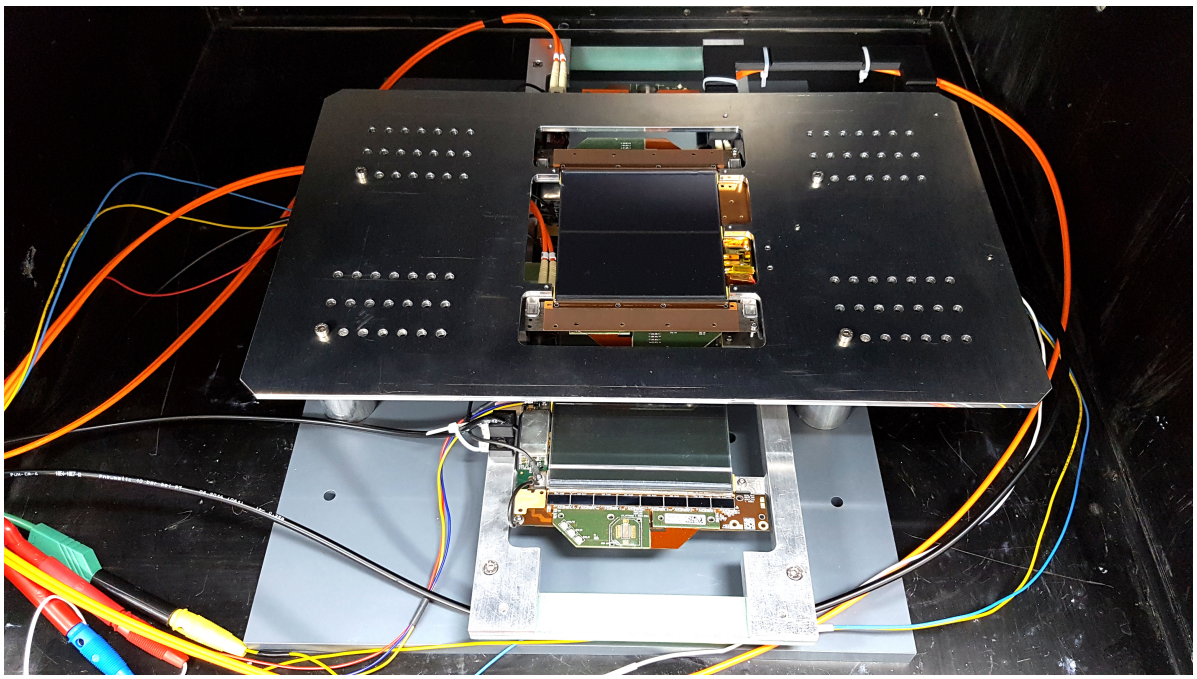

Figure 5.6.: Three modules mounted in the KALAMO barrel configuration. The lower modules are mounted face upwards on the ladder frame while the module mounted in the KALAMO carrier is oriented face downwards.

and is controllable with the Ph2_ACF readout software introduced in Section 3.3.3. The setup itself is mounted in a large box made of aluminum to protect the biased sensors from light. Figure 5.6 depicts the KALAMO barrel configuration equipped with three modules and placed inside the large box.

5.3. Noise Studies

Before taking data with test pulse injection, the noise of the modules mounted on the frame and the large carrier of KALAMO are investigated. The aim of these measurements is to find the grounding configuration with the lowest noise level.

To start the grounding study the module KIT_8CBC3_7 is mounted in the ladder frame. The noise is determined with a noise scan as described in Section 3.3.3. The number of events per threshold is set to 100. Different grounding configurations of the frame and the module are tested. Ground cables from the LV ground to one or both aluminum bars of the frame increased the mean noise of the module by around $1\,\mathrm{V_{CTH}}$. Therefore, no extra grounding cable from LV ground to the frame is used in the following noise tests and measurements. Connecting both aluminum bars with a cable does not change the noise. Thus, the electrical connection due to the Al-CF spacers is sufficient for data taking. Two grounding combinations of the module to the frame are investigated and can be seen in Figure 5.7. The first grounding configuration depicted in Figure 5.7(a) is realized by using two grounding cables at the module side opposite the SEH. One grounding cable is connected for each FEH. The second grounding combination depicted in Figure 5.7(b) mimics the grounding path of the 2S prototype modules. To avoid coupling of external noise, the module ground is separated via RC-circuit from the carrier ground. The noise is at the same level for both configurations. Thus, the grounding depicted in Figure 5.7(b) is used for the following measurements.

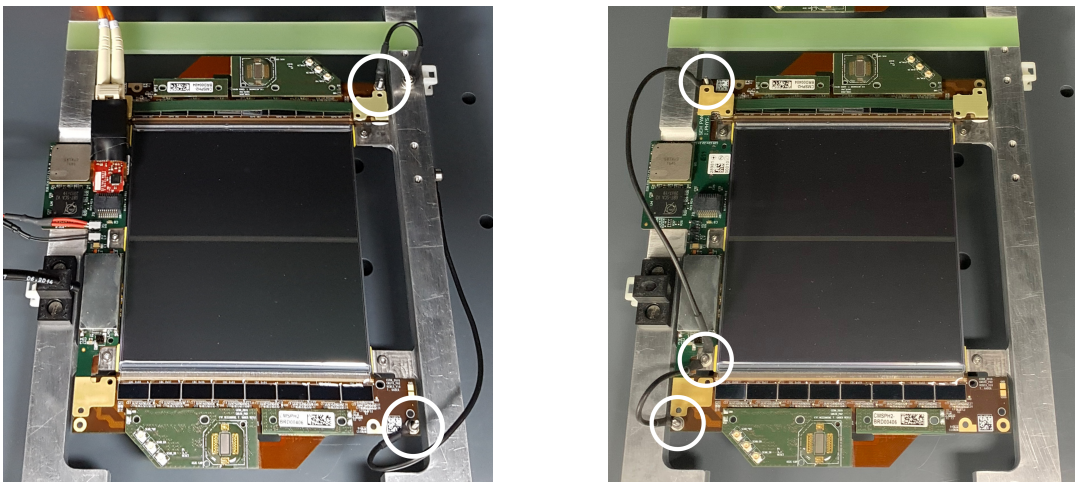

(a) Grounding at the SEH far side

(b) Grounding at the SEH side

Figure 5.7.: Grounding of the modules in the ladder frame of KALAMO. The grounding of the modules on the ladder frame is tested in two different configurations. (a) depicts the grounding configuration with two grounding cables attached at the SEH far side. The grounding configuration shown in (b) is mimicking the grounding path of the next hybrid version. The ground connections are indicated with white circles.

The noise with two and three modules mounted in KALAMO as depicted in Figure 5.6 stays at the same level as with one module. Plots of the noise corresponding to the situation where three modules are mounted are depicted in Figure 5.8. The mean noise is even slightly lower than in the 2S muon hodoscope depicted in Figure 4.10 where the modules are mounted on individual and isolated module carriers.

In conclusion, three 8CBC3 prototype modules were operated in a realistic electrical and mechanical arrangement and the mean noise was found to be on the expected level for each of them.

5.4. Test Pulse Injection

The CBCs can be triggered on internal test pulses as described in Section 3.3.2. The test pulses are injected in groups of channels. There are eight of these test pulse groups. To each test pulse group belong 15 or 16 strips per CBC, which corresponds to every eighth channel of each sensor. From the upper and lower sensor, the test pulses are injected in the channels where one is directly upon the other. The test pulses are used for the crosstalk measurements because it is an easy way to simulate the readout of data in modules.

The idea of the test pulse measurements is described in Section 5.4.1 while the test pulses are investigated in detail in Section 5.4.2. The results of further grounding studies are presented in Section 5.4.3 while the test pulse measurements are described in Section 5.4.4. The results of the first mounting of a 2S prototype module in the KALAMO box are shown in Section 5.4.5.

5.4.1. Idea of Test Pulse Measurements

The idea of the test pulse measurements performed with KALAMO is to generate electrical activity on two modules similar to operation conditions and to probe with a third module if it picks up any disturbances. During operation in the detector, some modules record hits from

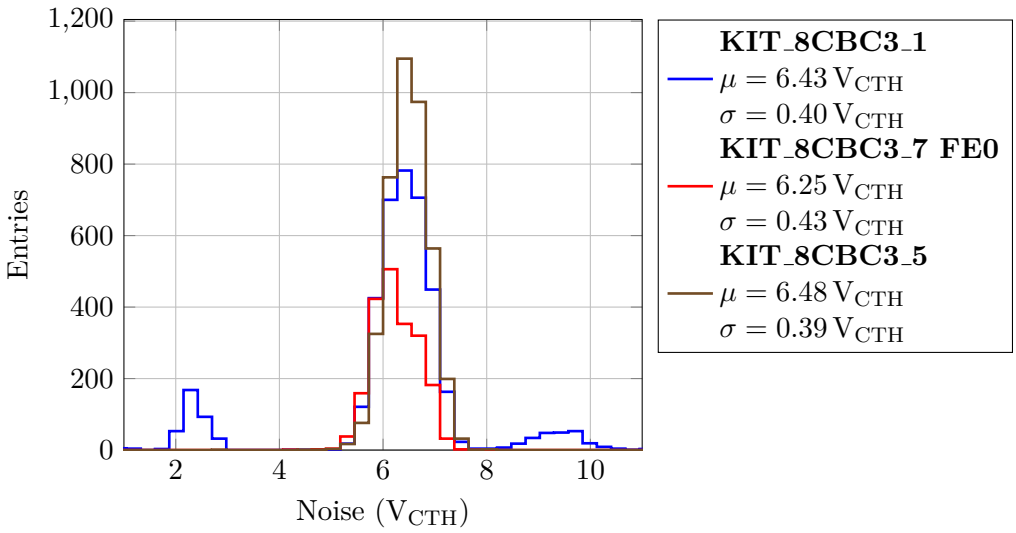

Figure 5.8.: Noise of KIT_8CBC3_1, KIT_8CBC3_7 and KIT_8CBC3_5 mounted in KALAMO. The noise level of all modules is nearly the same. The number of hits in the histogram of KIT_8CBC3_7 is smaller than of the others because the readout of FE1 failed. The left additional peak of module KIT_8CBC3_1 results from unconnected strips while the right additional peak results from some strips of the double length 10 cm.

traversing particles while others do not. To simulate this situation in the laboratory, hits are injected in two of three modules via test pulses and the third module is triggered on the trigger source of those internal test pulses as well, but there are no test pulses injected. The latency and stub latency of all three modules is set to the same value. They are determined from the latency scan with triggering on the internal test pulses. By switching on and off the test pulses in the modules from run to run, the influence of the readout electronics in operation on the third module can be measured. The hits in all three modules are recorded. Any influence of the modules electronics to the number of hits in the third one should be observed as an excess of hits in some channels. If there is an influence of the test pulse modules on the third module, the origin of the interference can be probed by changing the position of this third module with respect to the others.

5.4.2. Investigation of Test Pulses

First, the hit latency and stub latency of the injected test pulses is determined with the latency scan described in Section 3.3.3. The result plots are depicted in Figure 5.9. The latency and stub latency of test pulses show a peak over two clock cycles which means that the test pulses extend over two clock cycles. The latency is set to 75 clock cycles for hits and to 5 clock cycles for stubs.

To further investigate the behaviour of the test pulses, the first test pulse group is enabled while a simultaneous threshold and latency scan is performed. The test pulse delay is varied in 1 ns steps. Because this is performed at two latencies with 25 ns difference the test pulses are investigated over a range of 50 ns. The threshold is varied in 1 V_{CTH} steps. This measurement is performed for five different test pulse amplitudes between 160 V_{CTH} and 240 V_{CTH} in steps of 20 V_{CTH}.

The aim of this test pulse study is to extract the pulse heights $PH_{V_{CTH}}$ in units of V_{CTH} belonging to the different test pulse amplitudes $TPA_{V_{CTH}}$. For that purpose, the pedestal

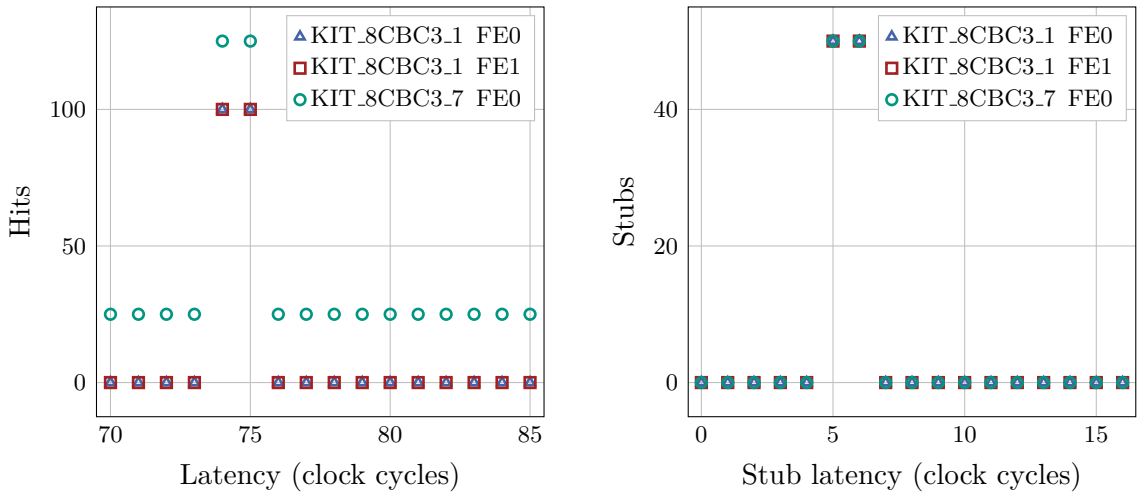

(a) **(b)**

Figure 5.9.: Latency and stub latency of KIT_8CBC3_1 and KIT_8CBC3_7 mounted in KALAMO. (a) shows the number of hits over the latency in clock cycles while (b) depicts the stub latency. The peaks indicate the correct latency. It is set to 75 clock cycles for hits and to 5 clock cycles for stubs. The excess of hits in KIT_8CBC3_7 FE0 results from CBC number 7, which was already broken before mounting the FEH in the module.

at each latency is estimated from the data. The first threshold with a hit occupancy larger than 50 % is taken as pedestal. Let $p_{\max}$ be the mean pedestal value at latencies without a test pulse. The value of $p_{\max}$ is calculated as the mean of the pedestals at the latencies before the test pulse starts. The minimum pedestal $p_{\min}$ is calculated from a quadratic fit around the minimum pedestals of the test pulse. The pulse height $PH_{\mathrm{V_{CTH}}}$ is than calculated as the difference $PH_{\mathrm{V_{CTH}}} = p_{\max} - p_{\min}$. The minimum is located at the latency with maximum test pulse height since the signal is negative due to electron readout. The results can be seen in Figure 5.10. The minimum pedestal is calculated via a quadratic fit around the test pulse maximum. Since this is performed for all channels with injected test pulses, the uncertainty of the pulse heights is given by the standard deviation of the pulse heights. A linear fit is performed to get a conversion formula

$$PH_{\mathrm{V_{CTH}}} = (1009.99 \pm 3.56)\,\mathrm{V_{CTH}} - (3.98 \pm 0.02) \cdot TPA_{\mathrm{V_{CTH}}} \tag{5.1}$$

from test pulse amplitudes in $\mathrm{V_{CTH}}$ to pulse heights in $\mathrm{V_{CTH}}$. The data point at a test pulse amplitude of 160 $\mathrm{V_{CTH}}$ is not used as fit input because the test pulse signal is so large that the analog chip frontend saturates.

With Equation (3.2) this formula can be expressed in units of electrons

$$PH_{\mathrm{V_{CTH}}} = (-4.43 \pm 5.58)\,\mathrm{V_{CTH}} + (0.0074 \pm 0.000031)\,\mathrm{V_{CTH}} \cdot \frac{TPA_{\mathrm{e^-}}}{\mathrm{e^-}}\,. \tag{5.2}$$

Rearranging Equation (5.2) yields the conversion from pulse heights in units of $\mathrm{V_{CTH}}$ to test pulse amplitudes in units of electrons

$$TPA_{\mathrm{e^-}} = (598.12 \pm 751.62)\,\mathrm{e^-} + (134.99 \pm 0.57)\,\mathrm{e^-} \cdot \frac{PH_{\mathrm{V_{CTH}}}}{\mathrm{V_{CTH}}}\,. \tag{5.3}$$

This formula is valid for test pulse amplitudes smaller than about 40,000 $\mathrm{e^-}$, for larger test pulses the analog chip frontend saturates.

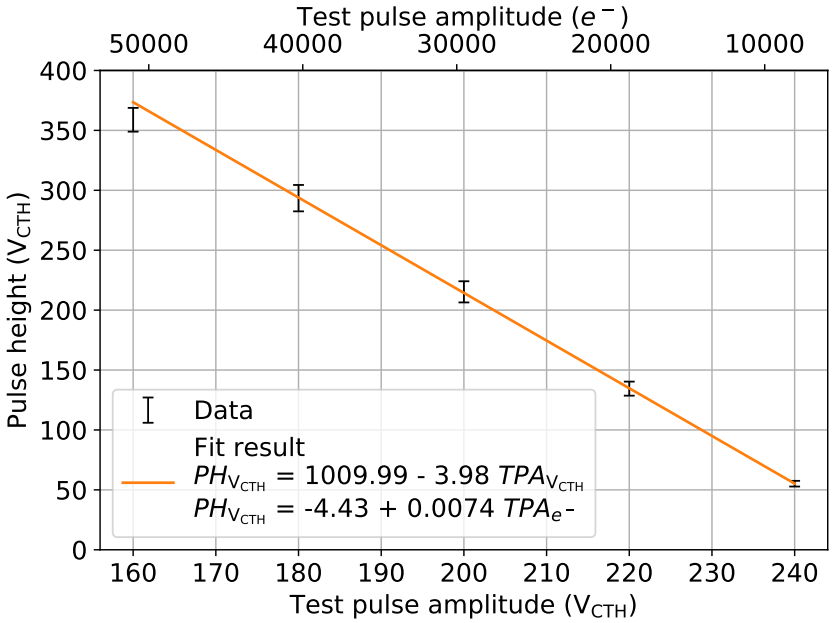

Figure 5.10.: Pulse height versus test pulse amplitude. The plot depicts the calculated pulse heights for the measured test pulse amplitudes. The error bars are given by the standard deviation of the different channels with injected test pulses. The two x-axes can be converted to each other via (3.2). The pulse heights lie in a straight line for large test pulse amplitudes. At a test pulse amplitude of 160 V_{CTH}, saturation occurs. Therefore, the linear fit is just performed for the other four data points.

The uncertainties of Equations (5.2) and (5.3) are given by the error propagation of the uncertainties of the fit parameters in Equation (5.1). With this method, the slopes are determined far more precisely than the intercepts.

For the following measurements, the test pulse amplitude is set to 214 V_{CTH} which corresponds via Equation (3.2) to a signal of 22,000 e^-. A signal of 22,000 electrons is the expected signal generated by MIPs in a 290 µm thick silicon sensor.

5.4.3. Grounding Studies

The following measurements are performed with an additional plastic platform under the baseplate of KALAMO. This is the result of measurements presented in Section 5.4.5 which show the reduction of environmental noise by this measure. All measurements of this section are performed with the module KIT_8CBC3_5 at a threshold $7 \times \sigma_{\text{noise}}$ away from pedestal. Since in between two runs a new calibration is performed, the threshold of different measurements is not always the same due to varying mean noise within the standard deviation between two runs. 5,000,000 events are recorded per run.

The working principle of the measurements described and performed within this subsection is to read out one module without any intentional signal injection and to count the noise hits in this module. The hit occupancy

$$\text{Hit occupancy} = \frac{\#\text{ of hits}}{\#\text{ of triggers}} \tag{5.4}$$

of each channel is then plotted over the channel number and can be compared to the number of expected hits per trigger and channel. The number of hits should result from the Gaussian noise of each channel. Depending on the threshold, the expected number of hits can be calculated. Measuring $6 \times \sigma_{\text{noise}}$ from pedestal, 3.4×10^{-6} hits per trigger are expected in contrast to 1.9×10^{-8} hits per trigger at $7 \times \sigma_{\text{noise}}$ from pedestal. The hit occupancy is used in the following as evidence for the module's grounding quality.

The first step to investigate the module's hit occupancy is to place the module mounted on its carrier in the module readout station described in [Kop18] and depicted in Figure 3.7. This is the setup normally used to read out modules. The hit occupancy measured with this configuration can be found in Figure 5.11. Since the hit occupancy is larger than expected for the measurement at a threshold of $7 \times \sigma_{\text{noise}}$ away from pedestal, the ground configurations have to be improved for further measurements at different positions of the KALAMO carrier.

For the next hit occupancy investigation, the module is mounted on the large KALAMO carrier and the resulting hit occupancy is compared with the expected hit occupancy resulting from Gaussian noise. In Figure 5.12, it can be seen that the hit occupancy is increased compared to the measurement in the module readout station by three orders of magnitude in FE0 and by two orders of magnitude in FE1. The number of hits is sloping down from its maximum at channel 0 to a small number of hits at channel 1015. The channel numbering of this analysis is as depicted in Figure 4.4, starting at the SEH far side with 0 and ending at the SEH near side with 1015. Different grounding configurations of the module to the KALAMO carrier and of the aluminum box to the laboratory ground are investigated to get the hit occupancy to the level reached on its carrier and to remove the asymmetric shape.

The influence of the aluminum cylinders on which the KALAMO carrier is mounted, is first tested. Removing them and mounting the large carrier normally orientated with up-facing module does not improve the hit occupancy. Grounding the aluminum box with a thick cable to the heating element of the laboratory does not improve the hit occupancy either. Rotating the module by 180° does also not change the shape of the background. As before, the channels far from the SEH see more noise hits than the others. Thus, this effect does not result from

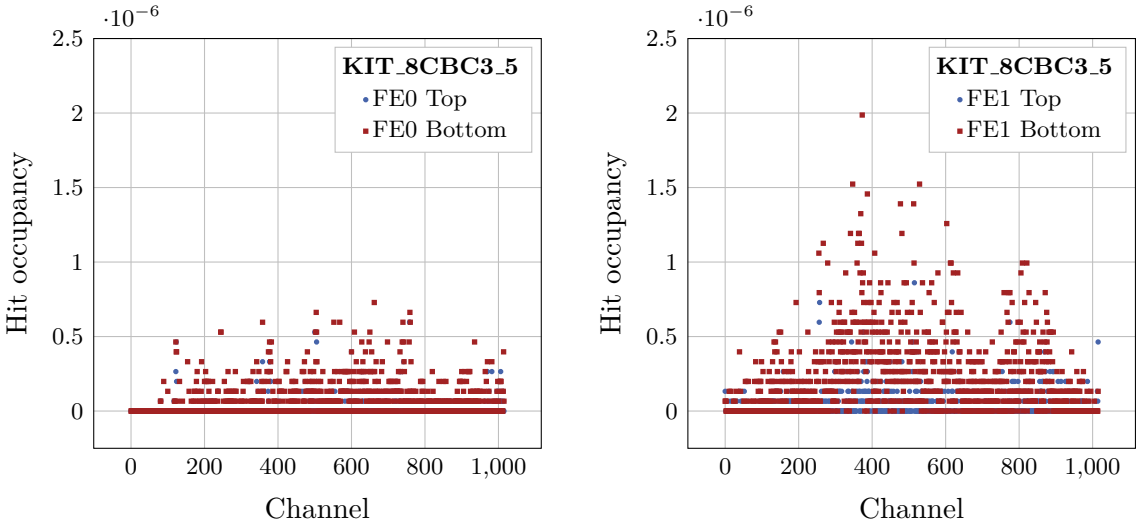

(a) FE0 **(b)** FE1

Figure 5.11.: Hit occupancy of KIT_8CBC3_5 mounted on its carrier in the KALAMO box. The hit occupancy of the module mounted on its carrier in the the KALAMO box is depicted for FE0 in (a) and for FE1 in (b). The number of hits is larger than expected from Gaussian noise.

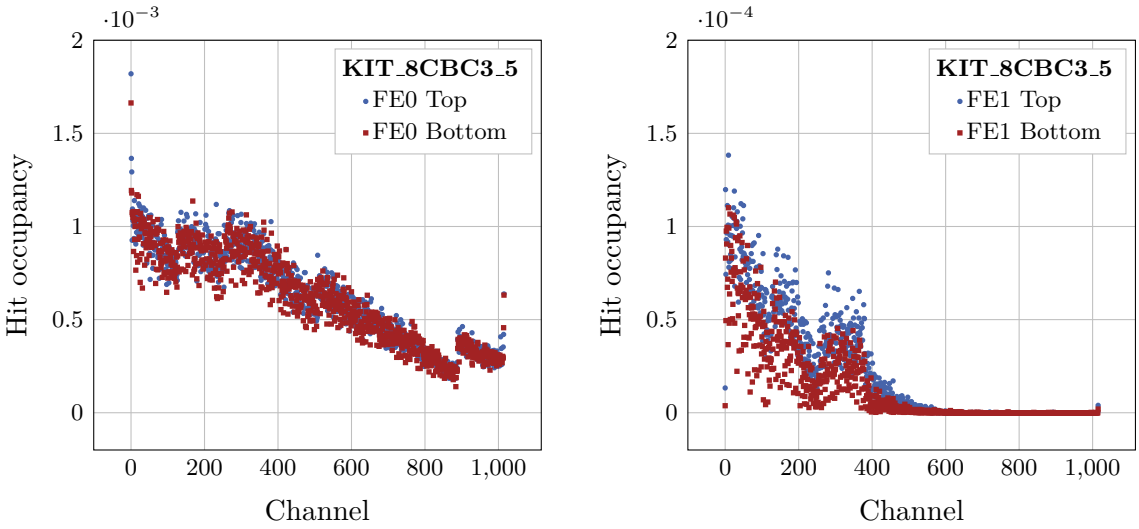

(a) FE0 **(b)** FE1

Figure 5.12.: Hit occupancy of KIT_8CBC3_5 mounted on the large KALAMO carrier. The hit occupancy of the module mounted on the KALAMO carrier is orders of magnitudes larger than mounted on the module carrier. The number of hits is decreasing from the SEH far side (channel 0) to the SEH near side at channel 1015. The number of hits is one order of magnitude larger in FE0 (a) compared to FE1 (b).

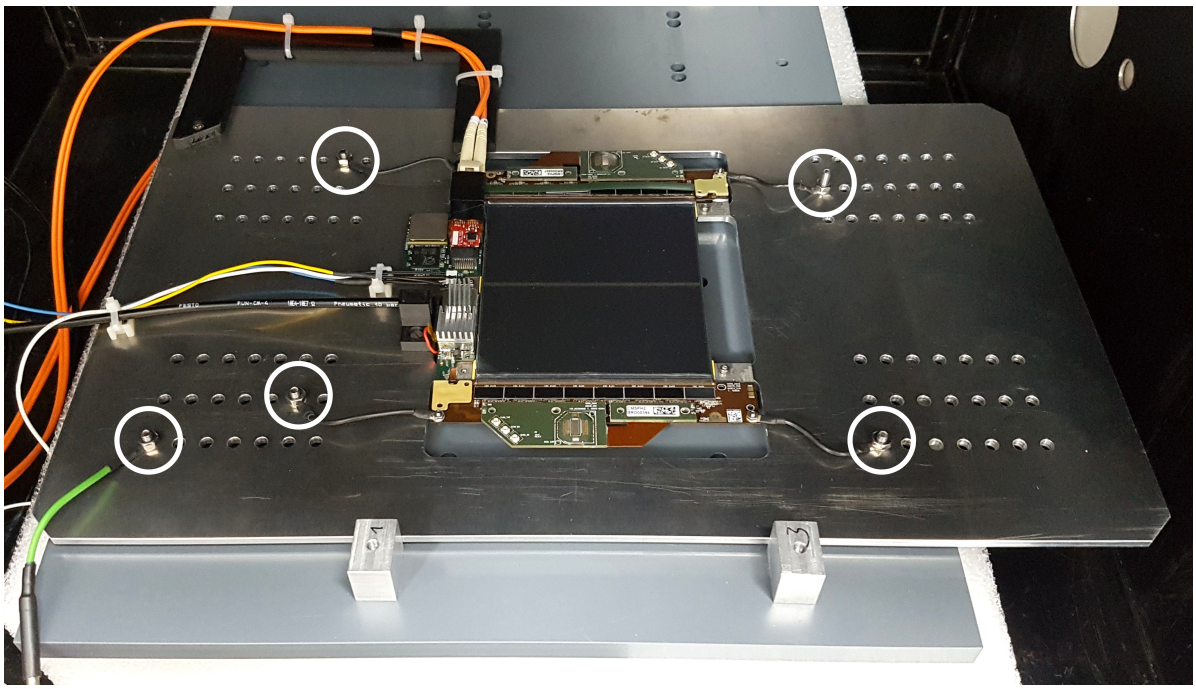

Figure 5.13.: Grounding of an 8CBC3 module on the KALAMO carrier. The grounding which leads to the smallest hit occupancy is realized with small cables from the grounding holes in the FEHs to the carrier. At the left bottom side in the picture, the green ground cable of the carrier to the LV ground can be seen. The grounding connections are indicated with white circles.

influences of the box since it is not changing with the orientation of the module with respect to the box. The large hit occupancy is assumed to result from not ideal grounding configurations of the carrier itself or the module to the carrier.

The grounding configuration of the module to the carrier used for the previously described measurements is depicted in Figure 5.7(b) and led to good noise results in Section 5.3. It is replaced by the configuration depicted in Figure 5.13. The module is grounded from the grounding holes to the carrier via cables. The cables are fixed to the KALAMO carrier with M4 screws to some holes of the hole pattern. Adding these cables to the SEH far side also results in reduced noise at the SEH far side, as shown in Figure 5.14. The noise of FE0 is two orders of magnitudes reduced while the noise of FE1 is in the same order but the hits are concentrated at the SEH near side in contrast to the situation before.

Adding an additional grounding cable from the LV ground to the KALAMO carrier leads to the hit occupancy depicted in Figure 5.15. The hit occupancy is in the same order of magnitude as the one reached with this module mounted on its carrier which is depicted in Figure 5.11. Since it is not expected to be able to reduce the hit occupancy lower than the one resulting from the configuration with the module mounted on its carrier, this configuration is used to perform the measurements presented in the next Section 5.4.4.

5.4.4. Measurements with Barrel Configuration

At different positions of the upper module with respect to the others, runs of 5,000,000 events each are recorded. A run with disabled test pulses is followed by a run with enabled pulses. These runs can be compared to check for possible influences of the test pulse injection. At each measured position, runs with all eight test pulse groups are recorded.

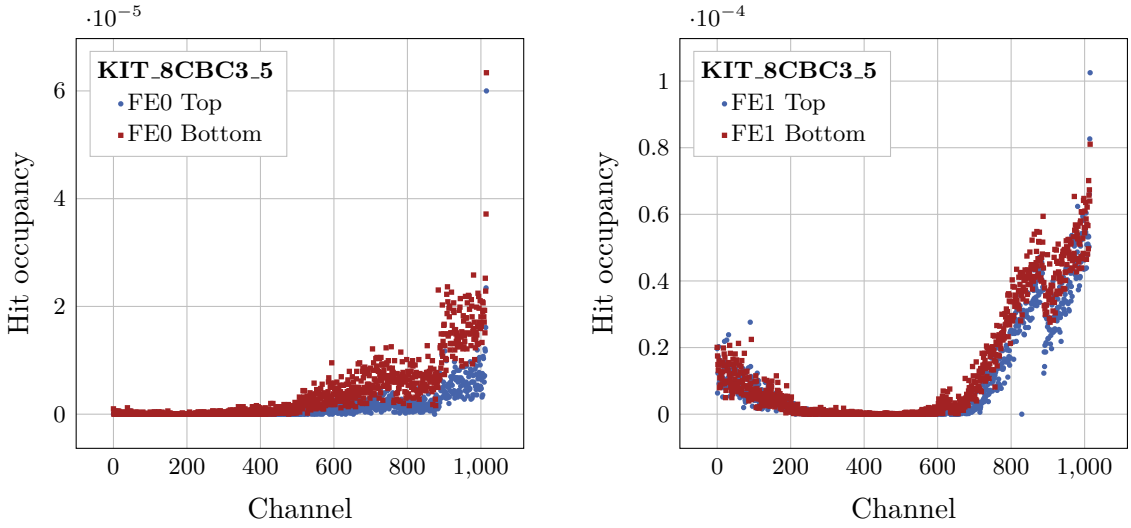

(a) FE0 **(b)** FE1

Figure 5.14.: Hit occupancy of KIT_8CBC3_5 mounted on the large KALAMO carrier with four ground connections via cables. The hit occupancy in FE0 (a) is reduced while the accumulation of hits in FE1 (b) is now located at the SEH near side.

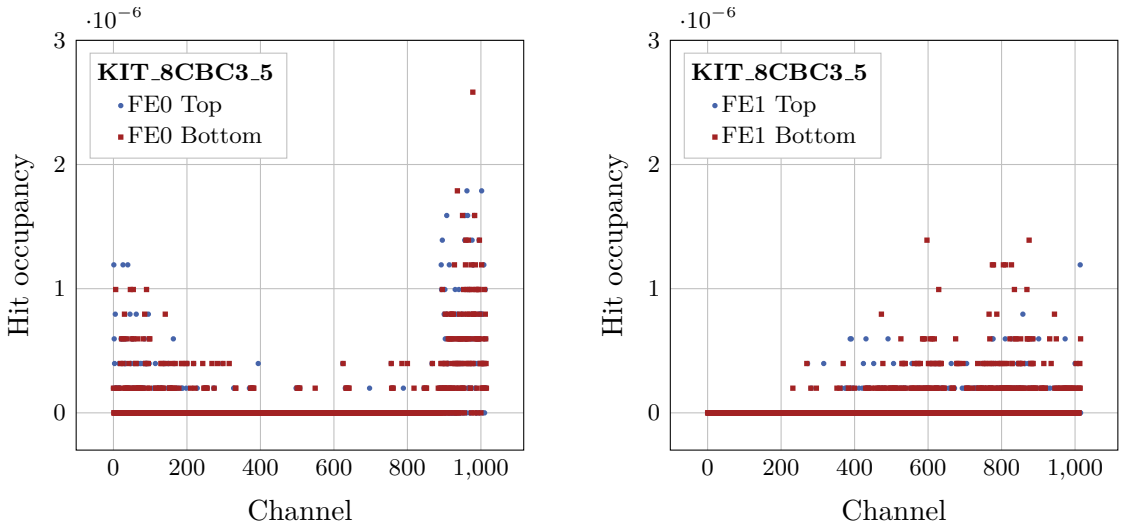

(a) FE0 **(b)** FE1

Figure 5.15.: Hit occupancy of KIT_8CBC3_5 mounted on the large KALAMO carrier with a grounding cable from the LV ground to the carrier. The hit occupancy with an additional grounding cable from the LV ground to the KALAMO carrier is in the same order of magnitude as if the module is mounted on the carrier depicted in Figure 5.11.

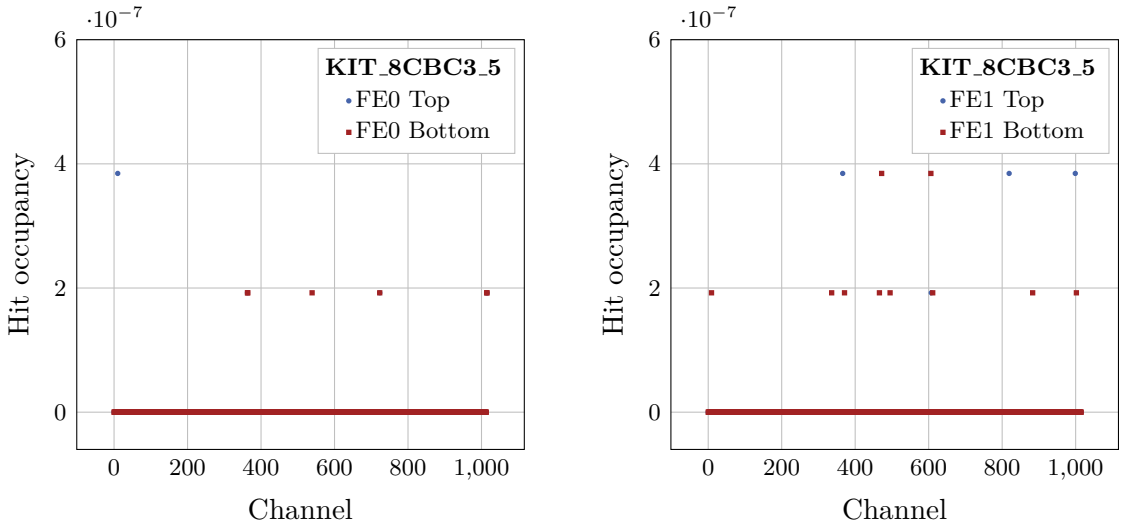

(a) FE0 **(b)** FE1

Figure 5.16.: Hit occupancy of KIT_8CBC3_5 at position (0 cm/0 cm). Occasional hits in all sensors are detected.

The positions are labeled according to their shift in x- and y-direction with respect to position (0 cm/0 cm). At this position, the sensor of the upper module is placed directly above the sensor of one lower module. The KALAMO carrier is mounted at position (0 cm/0 cm) in Figure 5.4 while position (10 cm/0 cm) can be seen in Figure 5.6. In x-direction a shift in 6 cm-steps is possible by the hole pattern in the base plate while the hole pattern in the carrier allows 2 cm-steps. The steps in y-direction are possible in six steps of one centimeter each.

The hit occupancy at position (0 cm/0 cm) can be seen in Figure 5.16. Single hits in some channels occur. The hit occupancy is smaller than measuring with the carrier lying on the baseplate (see Figure 5.15). This could result from the higher distance of the module to the ground due to the additional cylindrical legs under the KALAMO carrier. No influence of the lower modules to the upper is detected at this position. The hit occupancy shows no significant differences between the runs with different test pulse groups as well as the runs with or without enabled test pulses.

Shifting the module 12 cm in x-direction, no influence of the other module, which is then directly below, is detected at position (12 cm/0 cm). Moving the module also in y-direction, an excess of hits in the top sensor of FE1 is detected which can be seen in Figure 5.17. Moving the module to other y-positions (perpendicular to the strips), the excess moves the same distance as the the module is moved. With respect to the lower modules, the position remains the same. The excess at two other positions can be seen in Figures 5.18 and 5.19. Since the module is placed upside down, the top sensor is the sensor nearer to the lower modules. On top of the hit occupancy plot, the position of the upper module with respect to the lower modules is depicted. Figure 5.20 depicts the picture detail which is shown above the plots. The KALAMO carrier, the baseplate and the sensor of the module below FE1 of the upper module are taken out of the picture to see the position of FE1 with respect to the other modules clearer. The upper module is depicted transparent. The position of the excess is moving with the position of the upper module in y-direction. It is located above the aluminum bar of the ladder frame and the DC-DC converter of one of the lower modules. Due to the fact that the excess occurs in the data recorded with and without test pulse injections, it is more likely that this effect results from the aluminum bar of the ladder frame than from the lower modules. Nevertheless,

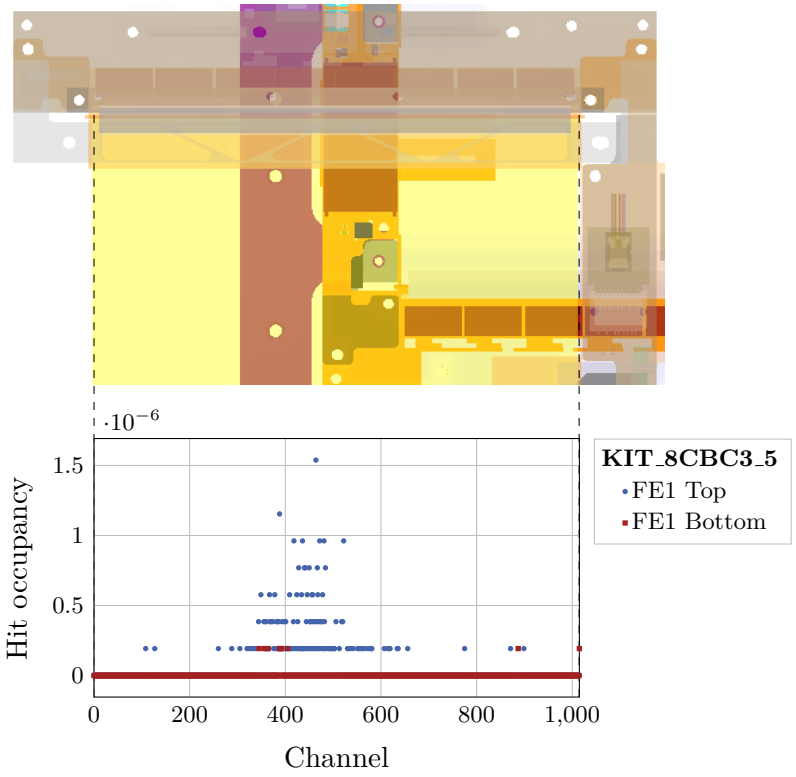

Figure 5.17.: Hit occupancy of KIT_8CBC3_5 at position (12 cm/6 cm). The hit occupancy shows an excess of hits which is located above the aluminum bar of the ladder frame and the DC-DC converter of one lower module. The x-axis is scaled to be comparable directly with the position with respect to the lower module. The upper module is depicted transparent.

the effect could come from the DC-DC converter because the LV was enabled in the case of disabled test pulses. In further investigations, the LV must be disabled, too, when disabling the test pulses to fully exclude the influence of electronic parts. To test the influence of the ladder frame, it is taken out of the KALAMO box and the other empty ladder frame is put in. However, after this change of the hardware, the observed module noise increased again without any obvious changes at the setup. This is a hint that the module is extremely sensitive to the grounding configuration in the KALAMO box, which needs to be further investigated.

5.4.5. First Tests With a 2S Module

The first measurements with a 2S prototype module are performed with the module KIT_2S_1. The module is mounted on its normal module carrier in the KALAMO box. As a first step, the noise is measured with the noise scan described in Section 3.3.3. The results can be found in Figure 5.21. With a mean noise of 7.40 V_{CTH} for FE0 and 7.17 V_{CTH} for FE1 the noise is about 1 V_{CTH} larger than the noise of an 8CBC3 prototype module. Performing the noise scan in the module readout station described in [Kop18] leads to a mean noise of approximately 7 V_{CTH}. A lower noise could not be reached with these modules and the origin of the increase in the noise compared to the 8CBC3 prototype modules has to be further investigated. The pedestal of the module of 600 V_{CTH} is at the same level as the pedestal of the 8CBC3 prototype modules. Therefore, the threshold of the measurements is set to higher values to take data also $7 \times \sigma_{noise}$ away from the pedestal. The latency of the injected test

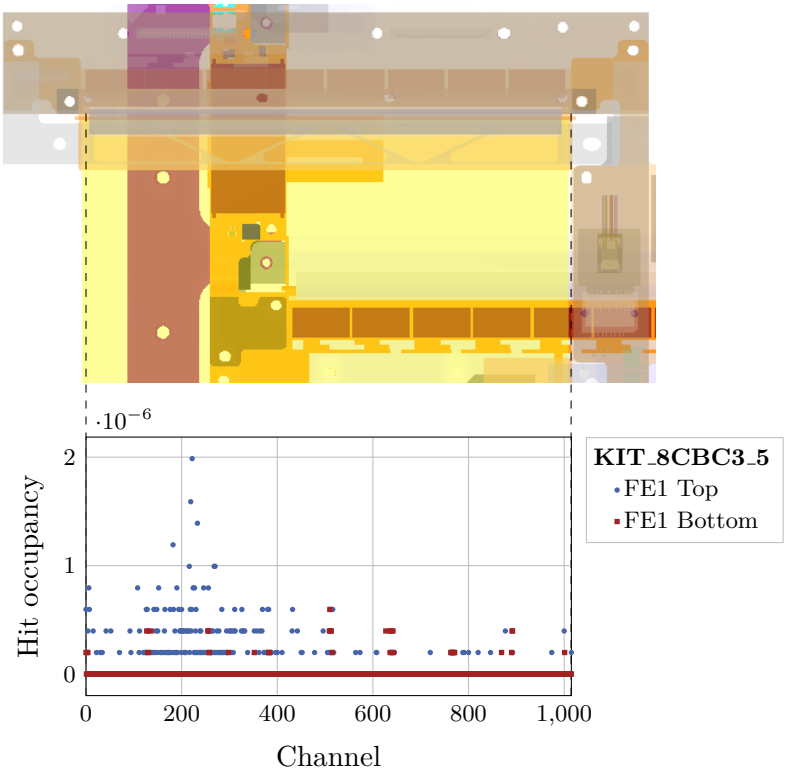

Figure 5.18.: Hit occupancy of KIT_8CBC3_5 at position (12 cm/4 cm). The hit occupancy shows an excess of hits which is located above the aluminum bar of the ladder frame and the DC-DC converter of one lower module. The x-axis is scaled to be comparable directly with the position with respect to the lower module. The upper module is depicted transparent.

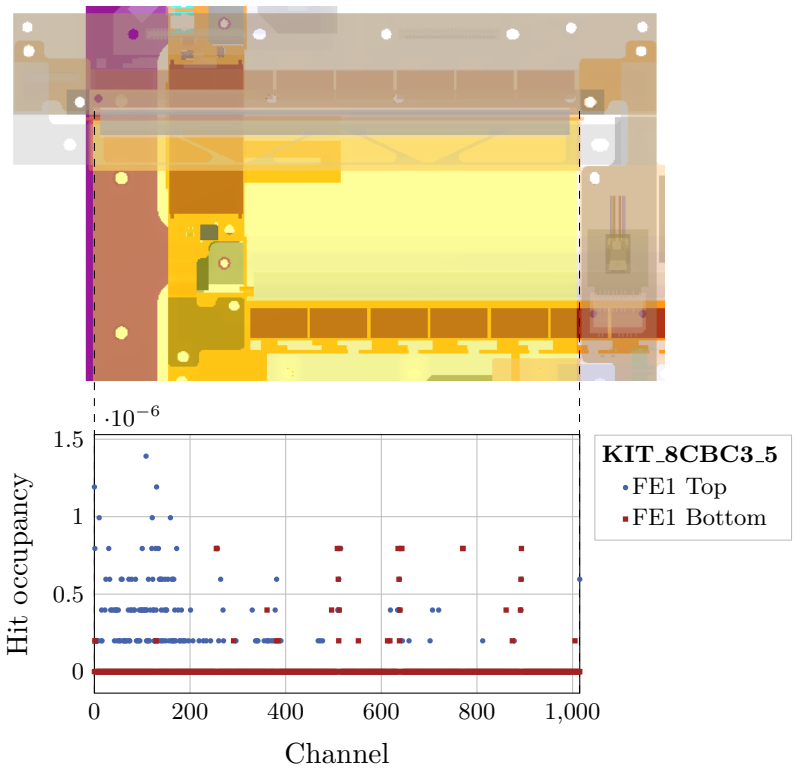

Figure 5.19.: Hit occupancy of KIT_8CBC3_5 at position (12 cm/3 cm). The hit occupancy shows an excess of hits which is located above the aluminum bar of the ladder frame and the DC-DC converter of one lower module. The x-axis is scaled to be comparable directly with the position with respect to the lower module. The upper module is depicted transparent.

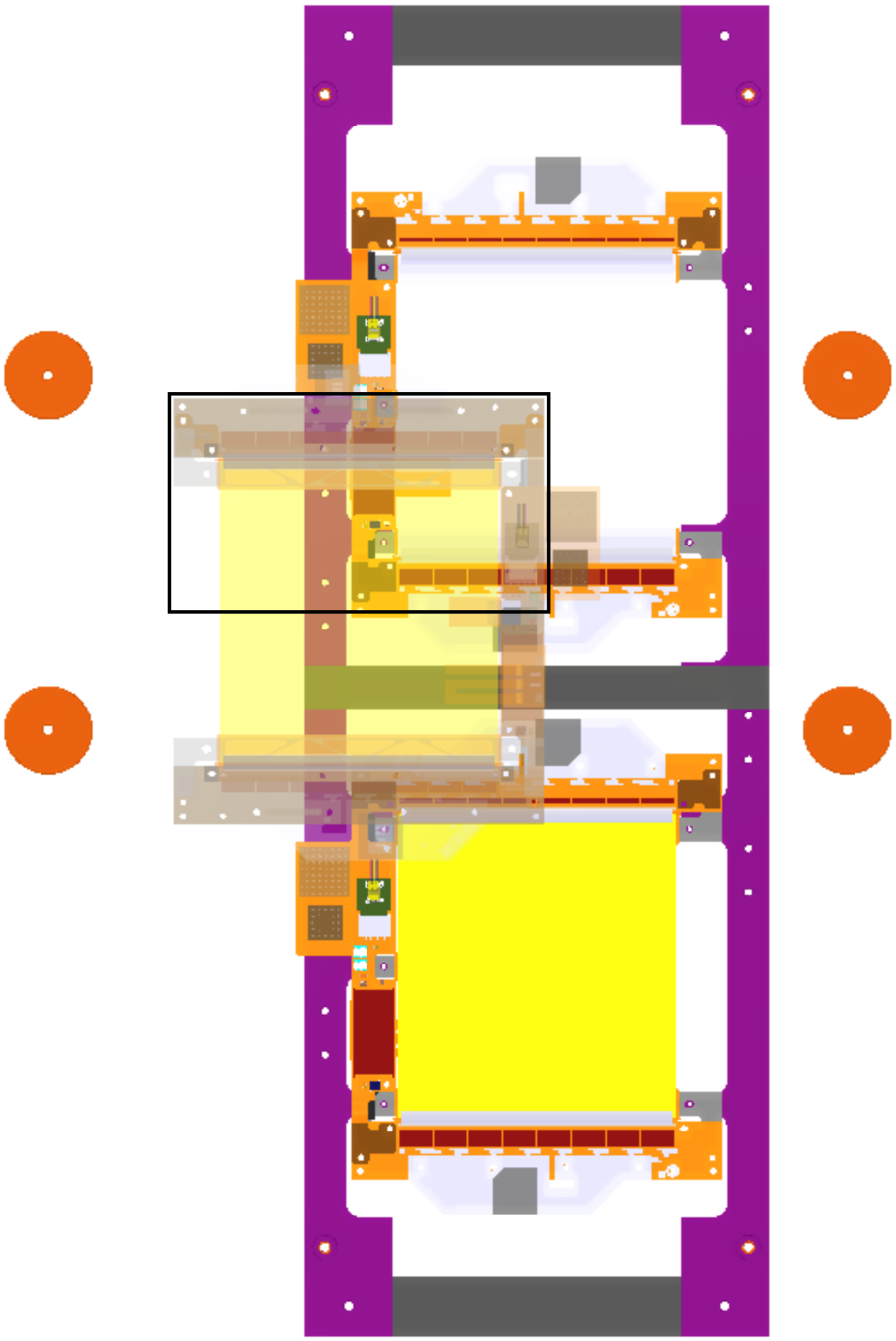

Figure 5.20.: Illustration of the KALAMO ladder structure with the upper module at position (12 cm/6 cm). The picture shows the KALAMO ladder structure without the baseplate and the KALAMO carrier. The upper module is mounted at position (12 cm/6 cm) and depicted transparent. The black rectangle depicts the cutout of the FE which shows the excess in the hit occupancy. The sensors of one lower module are removed.

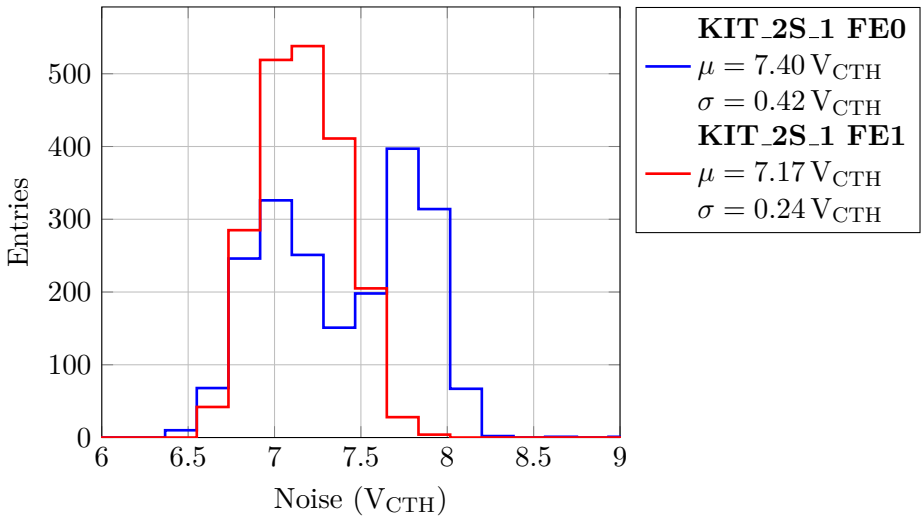

Figure 5.21.: Noise of KIT_2S_1. The mean noise of the 2S prototype module is approximately 7.3 $\mathrm{V_{CTH}}$. The noise of FE0 shows a double peak. The higher noise of FE0 results from the channels of the lower sensor.

pulses is determined from the latency scan as 200 clock cycles for hits and 136 clock cycles for stubs. The values are different compared to the latencies of the 8CBC3 prototype modules because new hybrid versions are built into the 2S prototype modules.

As a next measurement, the module is placed on the baseplate of KALAMO mounted on its carrier. Analog to the tests performed in Section 5.4.3, a run with 5,000,000 events is recorded. The hit occupancy of this measurement can be found in Figure 5.22. The number of hits in the upper sensor is five orders of magnitude larger than expected from the Gaussian strip noise. Since this is the case in the top sensor of the module when it is turned around, the effect could result from the aluminum baseplate of the box in which the experiment is mounted.

To test the influence of the aluminum baseplate on the number of hits, the baseplate of KALAMO is elevated with approximately 15 cm thick plastic. The hit occupancy of this measurement can be seen in Figure 5.23. The FEHs of the module see no hits except the bottom sensor of FE0. There are single hits in 5,000,000 events, which corresponds to a channel hit occupancy of approximately 8×10^{-7}. The occupancy of the whole module is 5.17×10^{-9} which is smaller than the expected number of 1.9×10^{-8} at a threshold of $7 \times \sigma_{\mathrm{noise}}$ away from pedestal. This arrangement with the additional plastic elevation below the KALAMO baseplate is the one used for the measurements described in Section 5.4.3.

The hit occupancy could be influenced by the aluminum of the baseplate and the ladder frame due to capacitative coupling. The aluminum parts act as an antenna. These effects are dependent on the quality of grounding of the aluminium parts. The better the grounding connections of the metal parts the smaller should be the influence of these metal structures on the module readout.

Next, noise studies have to be performed to investigate the higher mean Gaussian noise of the 2S prototype modules compared to the Gaussian noise of the 8CBC3 prototype modules. Also, grounding studies with 2S modules have to be performed analog to the measurements with 8CBC3 modules described in Section 5.4.3. For that the 2S modules will be mounted on the KALAMO carrier and the ladder structure of KALAMO, which is not yet done within this thesis. Due to the fact that the hit occupancy of one single 2S module mounted on a normal module carrier is extremely reduced compared to the hit occupancy of one single 8CBC3 module on a normal carrier it stands to reason that the hit occupancy of a 2S module mounted

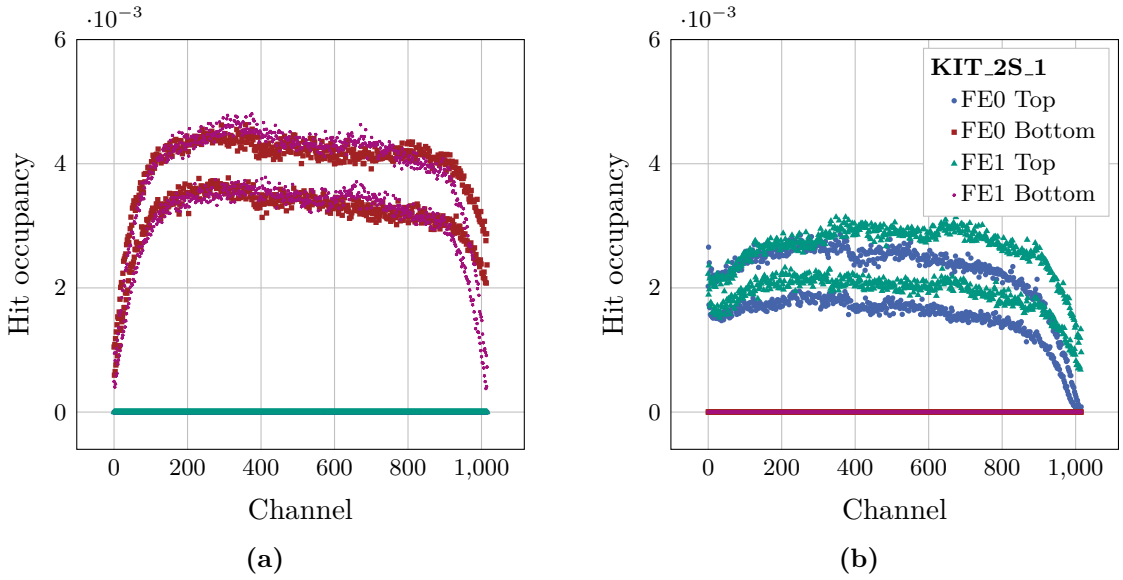

Figure 5.22.: Hit occupancy of KIT_2S_1 mounted on its carrier in KALAMO. In (a), the module is placed facing upwards while it is placed upside down in (b). A large number of hits is detected in the lower sensor (bottom sensor in (a) and top sensor in (b)). Some single hits are detected in the upper sensor.

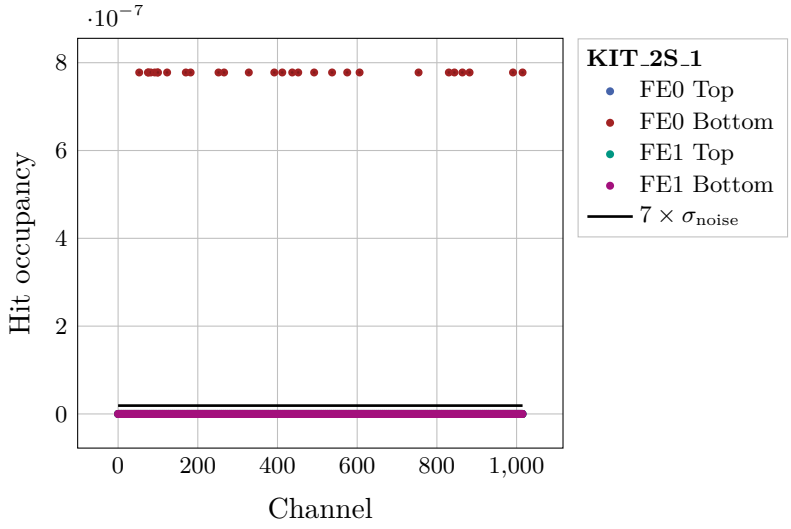

Figure 5.23.: Hit occupancy of KIT_2S_1 mounted on its carrier in KALAMO with an additional plastic plateau. The baseplate of KALAMO is elevated with an additional plastic plateau. The hit occupancy is zero except of some channels in the bottom sensor of FE0 in which single hits occur.

on the KALAMO carrier should be smaller, too. Thereby, hit occupancy excesses due to the possible influence of the other modules could be detected more easily. Further measurements with the final 2S prototype modules will follow, but are not part of this thesis.

Part III.

Summary and Outlook

6
Summary and Outlook

To be able to discover physics beyond the Standard Model of particle physics with the LHC, it will be upgraded to the HL-LHC until 2027. Due to the increased luminosity of the upgraded accelerator, the CMS detector has to be upgraded as well. The silicon tracker of the CMS experiment will be fully replaced. The new Outer Tracker of the *CMS Phase-2 Upgrade* will be equipped with 2S and PS modules. The silicon modules will be built at institutes of the CMS collaboration. The *Institute of Experimental Particle Physics* (ETP) at the *Karlsruhe Institute of Technology* (KIT) is one of the 2S module assembly centres. Within the last years, prototype modules were assembled at KIT. They are used to perform laboratory and integration tests.

In this thesis, the functionality of 2S modules was investigated with two setups: the 2S muon hodoscope and the *KArlsruhe LAdder MOckup* (KALAMO).

In the muon hodoscope, up to three 2S modules can be stacked on top of each other. Measurements with a single module were performed and the expected results were simulated. To compare the data of the measurements at fixed threshold with the simulation results, the conversion factor from the internal threshold units V_{CTH} to electrons is needed. It was extracted from the threshold scan data by the comparison between the measured cluster occupancy and the integrated simulated seed charge. A conversion factor of $176\,e^-/V_{CTH}$ resulted. Cosmic muons generate coincident hits in both sensor layers. The cluster size and the offset of the clusters in both sensors were investigated as well. The cluster size was equally distributed in both sensors and the offset distribution was as expected. Cosmic muons were also tracked with three modules read out synchronously. An alignment procedure was performed separately for both sensors of the middle module. Afterwards, the muon tracks were reconstructed with a linear fit to all cluster combinations in the six sensor layers. The measured incidence angle distribution followed the expected symmetrical shape centered around 0° and was decreasing for larger incidence angles. A dip in the number of hits at small negative angles was observed. This issue can also be seen in the correlation of the hits leading to the muon tracks. Entries in the diagonal, which represent vertically incident muons, were missing. Overall, the synchronous module readout succeeded. The problems which occurred during the measurements were most likely due to problems with the readout software and hence communicated to the software developers.

The distance between the modules in the new Outer Tracker of the CMS Phase-2 Upgrade is small to ensure hermetic coverage of the area around the collision point. The *KArlsruhe LAdder MOckup* (KALAMO) is a setup designed to simulate this arrangement of 2S modules in the future CMS Phase-2 Outer Tracker as well as to investigate grounding schemes and disturbances among the operated modules. The ladder structure can be simulated in the *ladder configuration* while the arrangement of modules mounted in neighboring ladders is mimicked in the *barrel configuration* of KALAMO. In the barrel configuration, the position of one module can be varied with respect to the others. If the sensing module picks up any disturbances of the other modules, the position can be changed to locate the origin of the disturbance. Both module prototypes currently assembled can be mounted in KALAMO despite different module outer dimensions. Measurements with 8CBC3 prototype modules mounted in the barrel configuration were performed. Test pulses were injected in the two modules mounted in the ladder frame

while the hit occupancy, which is defined as the number of hits over the number of triggers, was measured in the third upper module. An excess in the hit occupancy occurred independent of the test pulse injections. Most likely, the aluminum bar of the ladder frame or the shield of the DC-DC converter of one lower module were responsible for the disturbance. However, this could not be clarified definitely within this thesis. The measurements with KALAMO showed that the module performance is very sensitive to the grounding connections. Further measurements with the final 2S prototype modules will follow but are beyond the scope of this thesis.

As following measurements, 2S prototype modules should be mounted in KALAMO and a good grounding configuration should be found. The influence of the grounding of the metal parts has to be further investigated. The measurements have to be repeated with enabled and disabled test pulses as well as with passive modules with disabled low voltage. To check the influence of the aluminum parts of KALAMO, all modules except the sensing one have to be removed out of the setup. The configuration, which leads to a hit occupancy as expected from the Gaussian noise, has to be compared with the grounding in the later CMS Phase-2 Outer Tracker. If the results would hint that the planned grounding configurations are not sufficient, the CMS detector grounding has to be reconsidered in the context of the newest results.

In conclusion, within this thesis two setups to investigate the performance of 2S module prototypes were commissioned and first interesting measurements were performed that might hint to potential issues of the detector system.

Part IV.

Appendix

List of Figures

List of Tables

Bibliography

[Béj+20] I. Béjar Alonso et al. *High-Luminosity Large Hadron Collider (HL-LHC): Technical design report*. Ed. by I. Béjar Alonso. CERN Yellow Reports: Monographs. Geneva: CERN, 2020. DOI: 10.23731/CYRM-2020-0010 (cited on p. 8).

[Ben+04] M. Benedikt et al. *LHC Design Report Volume 3: the LHC Injector Chain*. CERN Yellow Reports: Monographs. Geneva: CERN, 2004. DOI: 10.5170/CERN-2004-003-V-3 (cited on p. 5).

[BR96] R. Brun and F. Rademakers. *ROOT - An Object Oriented Data Analysis Framework*. In: Nucl. Inst. & Meth. in Phys. Res. A 389 (1997) 81-86 (Sep. 1996) (cited on p. 20).

[Bra13] D. Braga. *CBC2 (CMS Binary Chip 2) User Guide 1.1*. Mar. 21, 2013. URL: http://www.hep.ph.ic.ac.uk/~dmray/CBC_documentation/CBC2_User_Guide_v1.1.doc (visited on 09/11/2021) (cited on p. 19).

[Bra20] J. Braach. *Functional Tests of 2S Detector Modules for the CMS Phase 2 Outer Tracker Upgrade including the Development of an IR LED Array*. Master's thesis. Karlsruhe Institute of Technology (KIT), 2020. URL: https://publish.etp.kit.edu/record/22024 (cited on p. 12).

[Brü+04] O. S. Brüning et al. *LHC Design Report Volume 1: the LHC Main Ring*. CERN Yellow Reports: Monographs. Geneva: CERN, 2004. DOI: 10.5170/CERN-2004-003-V-1 (cited on p. 5).

[Car+15] A. Caratelli et al. *The GBT-SCA, a radiation tolerant ASIC for detector control and monitoring applications in HEP experiments*. In: JINST 10 (2015), p. C03034. DOI: 10.1088/1748-0221/10/03/C03034 (cited on p. 19).

[CERa] CERN. *Linear accelerator 4*. URL: https://home.cern/science/accelerators/linear-accelerator-4 (visited on 09/25/2021) (cited on p. 9).

[CERb] CERN. *New technologies for the High-Luminosity LHC*. URL: https://home.cern/science/accelerators/new-technologies-high-luminosity-lhc (visited on 08/27/2021) (cited on p. 9).

[CER21] CERN. *The HL-LHC project*. Jan 2021. URL: https://hilumilhc.web.cern.ch/content/hl-lhc-project (visited on 06/21/2021) (cited on p. 8).

[CMS08] CMS Collaboration. *The CMS experiment at the CERN LHC*. In: Journal of Instrumentation 3.08 (Aug. 2008), S08004–S08004. DOI: 10.1088/1748-0221/3/08/s08004 (cited on p. 7).

[CMS17] CMS Collaboration. *The Phase-2 Upgrade of the CMS Tracker*. Tech. rep. CERN-LHCC-2017-009. CMS-TDR-014. CERN, Jun 2017. URL: https://cds.cern.ch/record/2272264 (cited on pp. 9, 10, 16, 17, 19, 21, 22).

[CMS21] CMS. *CMS Tracker Phase2 Acquisition & Control Framework*. May 2021. URL: https://gitlab.cern.ch/cms_tk_ph2/Ph2_ACF/-/releases (visited on 06/30/2021) (cited on p. 19).

[Dav16] S. R. Davis. *Interactive Slice of the CMS detector*. Aug. 2016. URL: https://cds.cern.ch/record/2205172 (visited on 09/30/2021) (cited on p. 7).

[Dem14] W. Demtröder. *Experimentalphysik 4: Kern-, Teilchen- und Astrophysik*. 4th ed. Springer, 2014. ISBN: 978-3-642-21475-2. DOI: 10.1007/978-3-642-21476-9 (cited on p. 14).

[Dem16] W. Demtröder. *Experimentalphysik 3: Atome, Moleküle und Festkörper*. 5th ed. Springer, 2016. ISBN: 978-3-662-49093-8. DOI: 10.1007/978-3-662-49094-5 (cited on p. 11).

[Dro18] A. Droll. *Characterization and Performance Study of Prototype Modules equipped with the CMS Binary Chip*. Master's thesis. Karlsruhe Institute of Technology (KIT), 2018. URL: https://publish.etp.kit.edu/record/21568 (cited on p. 14).

[Fel+17] L. Feld et al. *First Implementation of a two-stage DC-DC conversion powering scheme for the CMS Phase-2 outer tracker*. In: Journal of Instrumentation 12.03 (Mar. 2017). DOI: 10.1088/1748-0221/12/03/c03090 (cited on p. 19).

[Har17] F. Hartmann. *Evolution of Silicon Sensor Technology in Particle Physics*. 2nd ed. Springer, Nov. 3, 2017. ISBN: 978-3-319-64434-9. DOI: 10.1007/978-3-319-64436-3 (cited on pp. 13, 29).

[Hen10a] M. A. Hennig. *File:Schema - n-dotiertes Silicium.svg*. June 2010. URL: https://upload.wikimedia.org/wikipedia/commons/2/22/Schema_-_n-dotiertes_Silicium.svg (visited on 08/11/2021) (cited on p. 13).

[Hen10b] M. A. Hennig. *File:Schema - p-dotiertes Silicium.svg*. June 2010. URL: https://upload.wikimedia.org/wikipedia/commons/0/0d/Schema_-_p-dotiertes_Silicium.svg (visited on 08/11/2021) (cited on p. 13).

[Kop18] R. Koppenhöfer. *Conception and validation of test stations to electrically qualify silicon strip modules for the CMS Phase II Upgrade*. Master's thesis. Karlsruhe Institute of Technology (KIT), 2018. URL: https://publish.etp.kit.edu/record/21554 (cited on pp. 16, 18, 51, 56).

[Kul+19] S. Kulis et al. *A High-resolution, Wide-range, Radiation-hard Clock Phase-shifter in a 65 nm CMOS Technology*. In: Proceedings of the 26th International Conference "Mixed Design of Integrated Circuits and Systems" (2019), pp. 147–150. DOI: 10.23919/MIXDES.2019.8787202 (cited on p. 19).

[LR09] C. Leroy and P.-G. Ranciota. *Principles of Radiation Interaction in Matter and Detection*. 2nd ed. World Scientific Publishing, 2009. URL: http://www.gammaexplorer.com/wp-content/uploads/2014/03/RADIATION-INTERACTION-IN-MATTER-AND-DETECTION.pdf (cited on p. 16).

[Mai19] S. Maier. *Assembly and qualification procedures of 2S modules and high rate tests of the CMS Binary Chip for the Phase 2 Upgrade of the CMS Outer Tracker*. URL. PhD thesis. Karlsruhe Institute of Technology (KIT), 2019. URL: https://publikationen.bibliothek.kit.edu/1000104680 (cited on p. 30).

[Mob19] E. Mobs. *The CERN accelerator complex - 2019. Complexe des accélérateurs du CERN - 2019*. General Photo. July 2019. URL: https://cds.cern.ch/record/2684277 (visited on 08/29/2021) (cited on p. 6).

[Nod+18] B. Nodari et al. *A 65 nm Data Concentration ASIC for the CMS Outer Tracker Detector Upgrade at HL-LHC*. Tech. rep. Geneva: CERN, Oct. 2018. DOI: 1747420 (cited on p. 16).

[Pes+15] M. Pesaresi et al. *The FC7 AMC for generic DAQ & control applications in CMS*. In: Journal of Instrumentation 10.03 (Mar. 2015), pp. C03036–C03036. DOI: 10.1088/1748-0221/10/03/c03036 (cited on p. 19).

[Pry16a] M. Prydderch. *CBC3 Technical Specification*. May 16, 2016. URL: http://www.hep.ph.ic.ac.uk/ASIC/CBC_documentation/CBC3_Technical_Spec_V1p3.docx (visited on 09/11/2021) (cited on p. 19).

[Pry16b] M. Prydderch. *CMS Binary Chip Documentation*. May 2016. URL: http://www.hep.ph.ic.ac.uk/~dmray/CBC_documentation/ (visited on 07/05/2021) (cited on p. 19).

[Sch16] B. Schmidt. *The High-Luminosity upgrade of the LHC: Physics and Technology Challenges for the Accelerator and the Experiments*. In: Journal of Physics: Conference Series 706 (Apr. 2016), p. 022002. DOI: 10.1088/1742-6596/706/2/022002 (cited on p. 9).

[Tan+18] M. Tanabashi et al. *Review of Particle Physics*. In: Phys. Rev. D 98 (3 Aug. 2018), p. 030001. DOI: 10.1103/PhysRevD.98.030001 (cited on pp. 15, 27).

[Tro+17] J. Troska et al. *The VTRx+, an optical link module for data transmission at HL-LHC*. In: PoS TWEPP-17 (2017), 048. 5 p. DOI: 10.22323/1.313.0048 (cited on p. 19).

[Wyl+12] K. Wyllie et al. *A Gigabit Transceiver for Data Transmission in Future High Energy Physics Experiments*. In: Phys. Procedia 37 (2012), pp. 1561–1568. DOI: 10.1016/j.phpro.2012.02.487 (cited on p. 19).

Danksagung

Abschließend möchte ich mich bei allen bedanken ohne die diese Arbeit nicht möglich gewesen wäre.

Zuerst möchte ich mich bei Prof. Dr. Ulrich Husemann bedanken, der mir diese Masterarbeit durch die Aufnahme in die CMS Hardwaregruppe des Instituts für Experimentelle Teilchenphysik ermöglichte. Prof. Dr. Thomas Müller danke ich für die Übernahme des Korreferats.

Bei Dr. Alexander Dierlamm bedanke ich mich für die vielen hilfreichen Tipps während der Meetings. Roland Koppenhöfer danke ich für die exzellente Betreuung und dafür, dass er sämtliche Fragen zu jeder Zeit beantwortete.

Tobias Barvich und Marius Neufeld möchte ich für die wunderbare Hilfe beim Design, den Zeichnungen und dem Aufbau meines Setups danken.

Der gesamten ETP-Hardwaregruppe, insbesondere Tobias Barvich, Bernd Berger, Justus Braach, Dr. Alexander Dierlamm, Alexander Droll, Ronja Fischer, Prof. Dr. Ulrich Husemann, Roland Koppenhöfer, Dr. Stefan Maier, Prof. Dr. Thomas Müller, Jan-Ole Müller-Gosewisch, Marius Neufeld, Dr. Andreas Nürnberg, Dr. Hans Jürgen Simonis, Julian Stanulla, Pia Steck und Florian Wittig, danke ich für schöne Mittagspausen.

Meinen Eltern Silke und Marc Stockmeier, meinen Freunden und meiner Familie danke ich für Rückhalt und Unterstützung.